Combined Spectroscopic and Scanning Probe Studies of Electronic Interactions in Nanostructured 1D and 2D Semiconductors

Combined Spectroscopic and Scanning Probe Studies of Electronic Interactions in Nanostructured 1D and 2D Semiconductors

A Dissertation Presented

By

PEIJIAN WANG

Submitted to the Graduate School of the

University of Massachusetts Amherst in partial fulfillment

of the requirement of the degree of

DOCTOR OF PHILOSOPHY

May 2018

Department of Physics

Combined Spectroscopic and Scanning Probe Studies of Electronic Interactions in Nanostructured 1D and 2D Semiconductors

A Dissertation Presented

By

PEIJIAN WANG

Approved as to style and content by:

Michael D. Barnes, Chair

Anthony Dinsmore, Member

Ashwin Ramasubramaniam, Member

Narayanan Menon, Member

Narayanan Menon, Department Head
of Physics

DEDICATION

To my families,

Father Rongrui Wang, Mother Xianhua He

ACKNOWLEDGMENTS

First, I should express my sincere thanks to my advisor Professor Barnes. Many thanks for his many years of thoughtful, patient guidance and support. Because of your instruction, I can progress in the research. I also need to thank my committee members Professor Dinsmore, Ramasubramaniam, Menon for joining my PhD committee.

Second, I am thankful to my collaborator in Emrick group, Ryan Selhorst. Thanks for providing 2D materials to me and communication with me for the scientific thoughts and ideas. Collaborator in Kittilstved group, Dongming Zhou, through the talk and discussion of you, I learned a lot and our discussions incubate and catalyze some new ideas. Collaborator in DV group, Connor Boyle, I also learned a lot from you for the thermoelectric materials. Moreover, I express my sincere thanks to some fellows. Ned Burnett in the Polymer Science and Engineering, helped me to image tetraazaterrylene nanowires on the transmission electron microscope; Shaoyu Chen in Physics, helped to do the Raman spectroscopy and Photoluminescence upon doping for MoS_2 material. My labmate, Sarah Marques, I acquired some helpful information from you. Through the talk in the lab, we enhanced our friendship.

Finally, importantly, I am grateful to my families, my father Rongrui Wang, my mother Xianhua He. You consistently helped me in my way of life. Only with your support, I can make my way in the life.

ABSTRACT

COMBINED SPECTROSCOPIC AND SCANNING PROBE STUDIES OF ELECTRONIC INTERACTIONS IN NANOSTRUCTURED 1D AND 2D SEMICONDUCTORS

MAY 2018

PEIJIAN WANG, B.S. PEKING UNIVERSITY

Ph.D. UNIVERSITY OF MASSACHUSETTS, AMHERST

Directed by: Professor Michael D. Barnes

My dissertation work focuses on the questions of how the structural factors like the order and doping influence the electronic properties of materials. Specifically, the questions and the material platforms mainly include two aspects: In organic semiconductor assemblies, how the work function correlates with the π stacking order and the ground state charge transfer (CT) couplings. In inorganic material transition metal dichalcogenides (TMDC), how non-covalent chemical doping tunes the work function. Other than these, we also investigated about the 0D aluminum doped ZnO nanocrystal with the questions whether there are surface charges in the AZO nanocrystals and how the surface charge and polarizability evolve from undoped to doped

AZO. The work function is the energy associated with promoting an electron from the Fermi level (electron chemical potential) to the vacuum level, and it determines the charge transport and excitation properties. The experimental apparatus I used is the integrated spatially-registered Kelvin Probe Force Microscopy with photoluminescence (PL) spectroscopy. The KPFM exploits the capacitive interactions between the metallic-coated probe and the material under investigation, and detects the Fermi level of material, with a spatial resolution determined by the probe nominal radius (20~30nm) and an energy resolution of a few meV. The photoluminescence spectra result from the electron transition in the band structure. Structural factors like the order in organic semiconductors and doping in two-dimensional materials display signatures in the PL. Combination of them offer a powerful tool to correlate the electronic properties of materials to the order and doping. The first work is to explore the manifestation of ground state charge-transfer (CT) couplings in the work function in the ordered 7,8,15,16-tetraazaterrylene (TAT) assemblies. The photoluminescence spectra in organic semiconductors contains the information about both the Frenkel Exciton couplings (FE) "bright" and Charge Transfer (CT) "dark" couplings. They cannot be separately evaluated through barely the PL spectra. Capable to detect the "dark"-coupling-perturbed Fermi level, integration of the KPFM onto the PL provides a means to disentangle the "bright" and "dark" couplings. TAT is a superior material platform for this study due to i). Long-range FE couplings and short-range CT couplings coexist. ii). Its theoretically simulated spectra were established. iii). The spiral arrangement minimizes the intra-plane couplings, leaving only the couplings along the π stacking axis. My research found that the order decreases the work function, resulting from the ground state CT-couplings, and revealed the indication of the magnitude of charge transfer couplings. Since the work function in the organic semiconductor governs the charge injection/extraction in the interfaces and the harvestable photovoltage directly, this study is intensely conducive to the work function engineering of organic semiconductors. 2. Furthermore, modification of the TMDC work function using mechanical strain, heterostructure fabrication, or transition metal substrates has been reported. However, these methods are cumbersome, typically involving complicated deposition protocols or use of extremely expensive substrates. Non-covalent chemical doping points to a convenient route for tailoring electronic properties of TMDC. With the aim to find how the non-covalent chemical doping tunes the work function of TMDC, the KPFM was used to study the Fermi level change of MoS_2. In my research, bidirectional tuning of the Fermi level of MoS2 was achieved with large shifts through non-covalent chemical doping, with the PL spectra further verifying the n- and p-doping. This research discovered how the doping and substrate selection influence the work function change with clear manifestations, and benefits the device engineering of the TMDC materials. 3. Moreover, some work about semiconductor nanocrystals is also accomplished. Hetero-valent doped like Aluminum doped ZnO (AZO) nanocrystals has higher carrier concentration than the bulk and unique defect chemistry. Model about the charges of AZO were established, and has implications of the surface charge due to wavefunction expansion and stabilization of carriers. The Electrostatic Force Microscopy (EFM) was employed to provide direct evidence for the surface charges in the AZO nanocrystals and also the polarizability was measured, leading to verification of highly active dopants percentage, and the knowledge of the electron distribution in the nanocrystals. Since charge can significantly influence the optoelectronic and catalysis properties, and is associated with the luminescence dynamics like blinking, it expands the possible utility of the AZO system. Besides, the combined KPFM and PL technique was used to probe how distribution of the surface density of states is like in the organic thermoelectric materials in the process of doping with iodine and striking inhomogeneity is discovered, contributing to more thorough understanding of the charge transport process and efficiency enhancement in organic thermoelectric materials. These works demonstrated the power of the KPFM applicable to different areas: for the work in organic semiconductors, it is profoundly impactful on the optimizing organic semiconductor devices for energy/charge transport through packing motifs; as for the 2D TMDC work, it is helpful to scalable integration and exercising greater control onto TMDC; and for the nanocrystal work, it is beneficial to the potential application of nanocrystals in the smart windows or the luminescence source.

TABLE OF CONTENTS

Page

LIST OF FIGURES

Figure Page

CHAPTER 1

INVESTIGATION OF COMBINED "BRIGHT" and "DARK" INTERACTIONS IN ORGANIC SEMICONDUCTOR ASSEMBLIES

1.1 Introduction and overview of the first project

Organic semiconductors stimulate high enthusiasm of research worldwide, owing to possessing the characteristics such as light weight, biocompatibility, low cost, optoelectronic tunability and

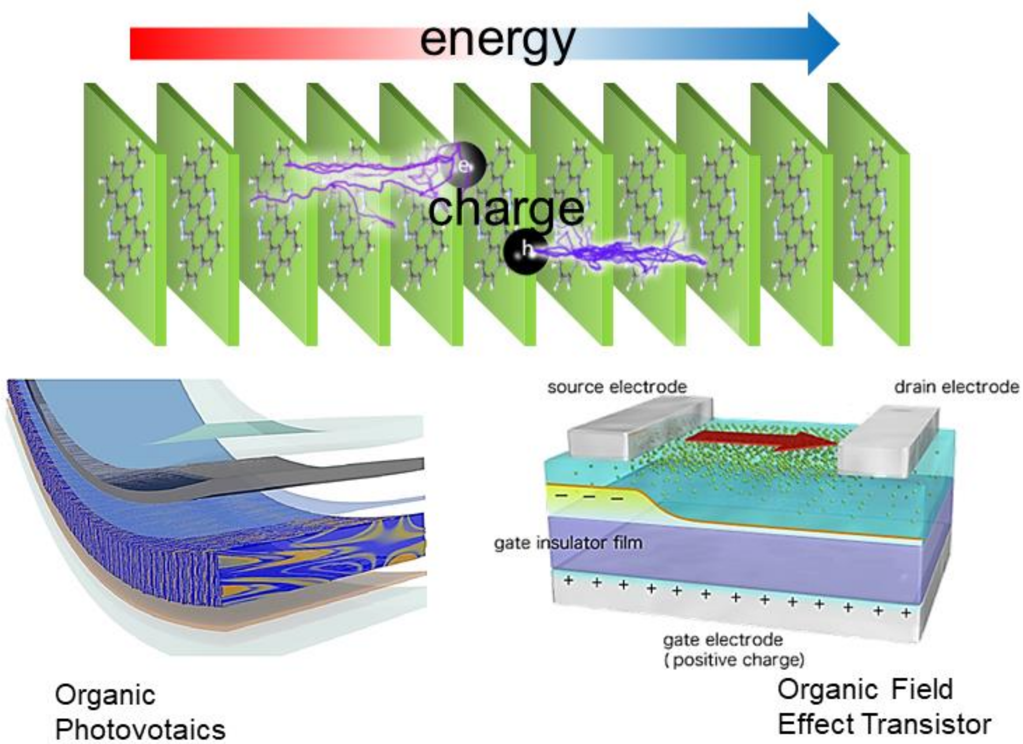

Figure 1. The schematics of the research theme of directional energy and charge transport. The potential applications such as OPV and OFET are also illustrated here.

flexibility.[3-4] The potential applications such as organic field effect transistors (OFET), organic light emitting diodes (OLED), organic photovoltaic (OPV), molecular electronics, flexible electronics, drive science community to devote extensive efforts into this area.[5-8]

Figure 1 illustrates the research theme of exploration of the connection of the packing motifs and the electronic properties in organic semiconductors in my studies, which is helpful in the research in directional energy/charge transport, and also the structures of some of the applications of organic semiconductors. The “Golden Rule” in materials science: The properties including mechanical, electronic, optical ones etc. are determined by the structures, also applies in the organic semiconductor materials. Molecular-scale structures impact the function-essential processes including exciton generation, dissociation, transport, diffusion and recombination in organic semiconductors.[9] Some knowledge about the connection between the molecular-scale structure and its manifestation in the spectroscopic features had been established. Kasha proposed a model in 1970s, which takes into account of the Frenkel Exciton (FE) couplings.[2]

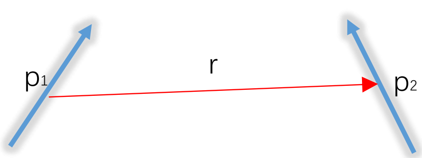

Figure 2. The schematic of dipole-dipole interactions (FE). The dipoles are noted by p_1 and p_2.

Figure 2 illustrates the FE couplings between two dipoles. When the excitation light transmits through the organic semiconductor, it generates electron and hole pairs (excitons), forming dipoles. The FE coupling between the dipole and dipole, possess an energy of

$$J = \frac{1}{4\pi\varepsilon_0 r^3}\left(\overrightarrow{p_1}\cdot\overrightarrow{p_2} - 3(\overrightarrow{p_1}\cdot\hat{r})(\overrightarrow{p_2}\cdot\hat{r})\right), \tag{1.1}$$

where $\overrightarrow{p_1}$, $\overrightarrow{p_2}$ are the dipole vectors, $\hat{r}$ is the unit vector along the displacement between the centers of two dipoles (Figure 2). By equation 1.1, the colinear (or "head to tail") or the cofacial (or "face to face") configurations lead to respectively negative or positive coupling energies. In this model by Kasha, the well-known excited-state ("bright") interaction give rise to the so-called H or J aggregate spectral features, manifested as a

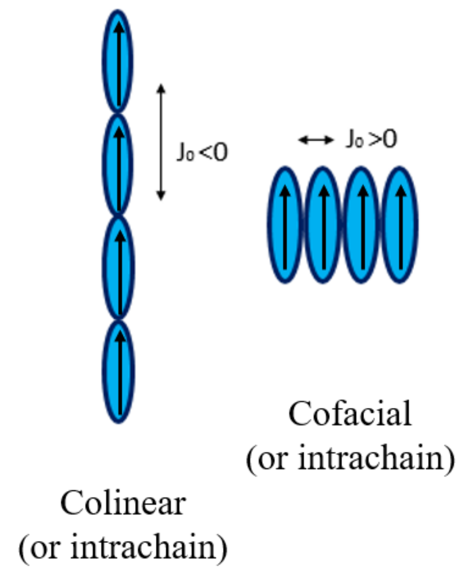

Figure 3. The colinear (Left) and cofacial (Right) chromophores configurations. The black arrows indicate dipoles. The coupling energy for the colinear configuration is negative, and for the cofacial case is positive.[2]

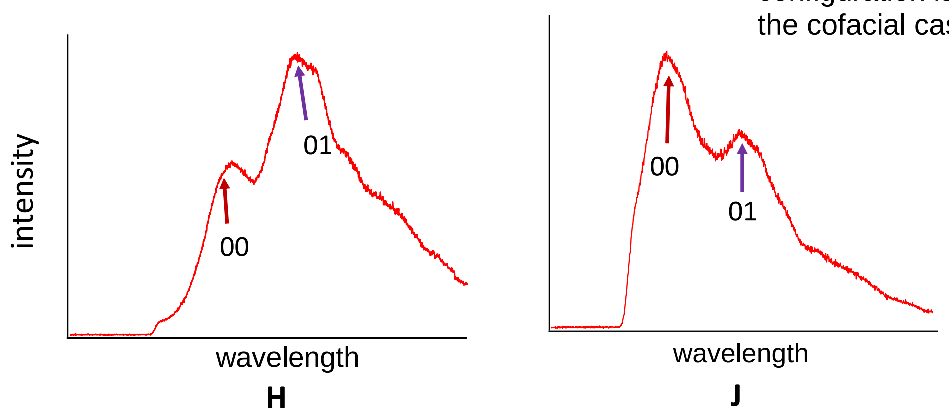

Figure 4. The sample spectra of the H aggregate (Left) and the J aggregate (Right) respectively. The peak indices are labeled. The H spectrum shows a smaller than 1 I_{00}/I_{01} intensity ratio and the J spectrum shows a greater than 1 I_{00}/I_{01} intensity ratio.

relative diminution or enhancement of 0-0/0-1 intensity ratios in the cofacial or colinear stacking, whose reason will be explained in the following. Representative spectra of the J and H aggregates with intensity ratios smaller or greater than 1 are shown in Figure 4.

The explanation for the I_{00}/I_{01} intensity ratio can be two-fold. The first understanding is by the transition dipole moment (TDM) and is shown in Figure 5. The coupling energy $J_{coupling}$ for the H

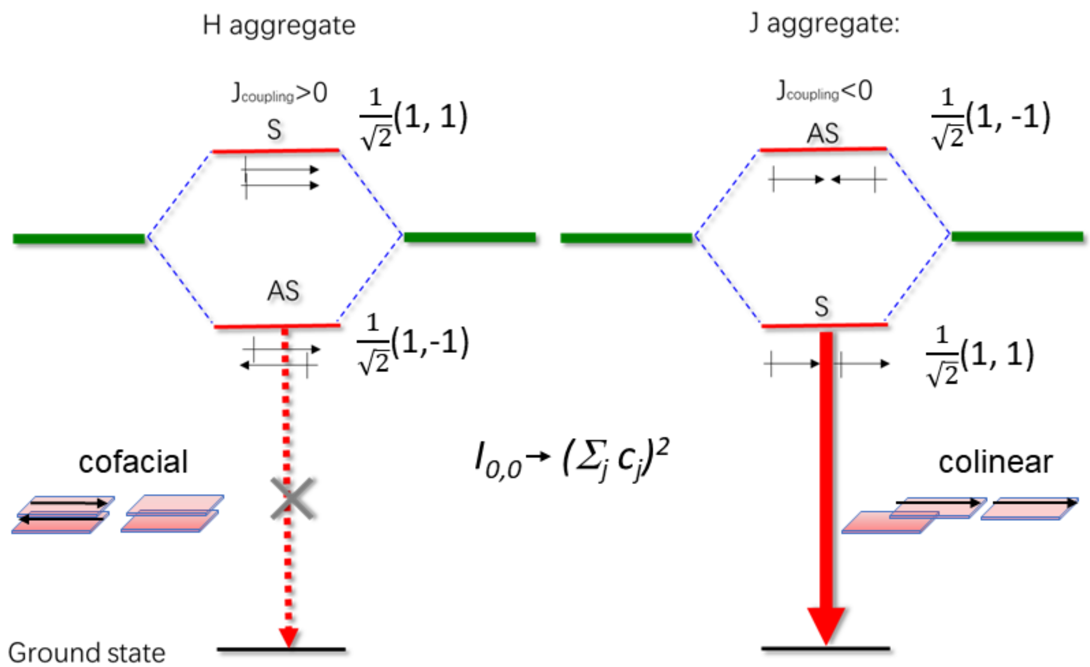

Figure 5. The schematic for understanding of the H and the J aggregates by the transition dipole moment. In the H aggregate, the site symmetry of the dipoles is anti-symmetric (AS), leading to a zero total transition dipole moment. In the J aggregate, the site symmetry of the dipoles is symmetric (S), leading to a non-zero total transition dipole moment.

aggregate in a dimer is positive, the lowest energy state will be antisymmetric arrangement of dipoles for the cofacial configuration, leading to a total zero transition dipole moment. Thus, the I_{00} transition is optically theoretically "forbidden", producing a smaller than 1 I_{00}/I_{01} ratio. On the other hand, the coupling energy for the J aggregate is negative, causing the lowest energy arrangement to be symmetric, leading to a total non-zero transition dipole moment.[10] Thus, the I_{00} transition is theoretically allowed and preferred (sometimes called "superradiant"), producing a greater than 1 I_{00}/I_{01} ratio (Figure 4). The second understanding roots in that the coupling energy alters the band curvature (Figure 6). The energy band of J aggregate bends down, the exciton stays at k=0 in the lowest excited state. Thus 00 transition is allowed and more favored than 01 transition, thus $I_{00}/I_{01}>1$. Otherwise, the energy band of H aggregate bends up, after the relaxation process, the exciton swings to k≠0.

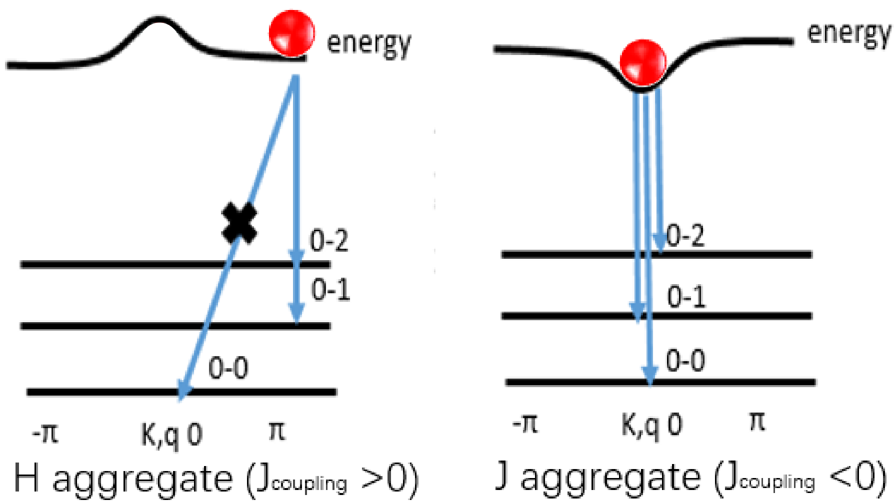

Figure 6. The schematic for understanding of the H and the J aggregates by the band curvature. The energy band bends up for the H aggregate (The exciton stays at k≠ 0, and bends down for the J aggregate (The exciton stays at k=0).

Therefore, the 00 transition is unfavored due to momentum conservation, and hence $I_{00}/I_{01}<1$.[2] Moreover, according to literature, the intensity ratio can be used to directly extract the exciton coupling strength by

$$\frac{I_{Abs}^{00}}{I_{Abs}^{01}} \approx \left(\frac{1-\frac{0.24W}{\hbar\omega_0}}{1+\frac{0.73W}{\hbar\omega_0}}\right)^2, \text{where } W = 4J_{coupling,}\ \ \hbar\omega_0 = 180meV, \qquad (1.2).^2$$

Therefore, the intensity ratio reflects the packing motif and the exciton coupling strength, and functions as an indication of the structural information.

Although Kasha's model can explain some of the polymer's spectral property, it is not thorough and does not take the complexity and imperfections in the organic semiconductor into account and is incapable to explain the spectral behavior of many aggregates. Examples include nanopillars of 7,8,15,16-tetraazaterrylene, as well as several perylene-based dyes, which exhibit H-to J-aggregate conversions, along with the slide between chromophores. More recent theoretical and experimental work, such as by Yamagata and Spano, point to a more complex picture of the exciton coupling which is mediated by both the Frenkel Exciton coupling (FE) and the Charge Transfer coupling (CT).[9] The Charge Transfer coupling can also give rise to the H and J aggregate. When the electron transfers from one chromophore to an adjacent chromophore and leaves a hole, the charge transfer couplings occur. The CT couplings do not call for the exciton excitation and can occur in dark, leading to the name of “dark” couplings, while the FE couplings call for the exciton excitation and lead to the name of “bright” couplings. The CT couplings can lead to H and J spectral classification as well because it also has a positive or negative coupling energy.

The Hamiltonian including both the FE and CT couplings becomes:

$$H = \hbar\omega_0 \sum_{n=1,2} b_n^+ b_n + \hbar\omega_0 \sum_{n=1,2}\{\lambda(\hat{b}_n^+ + \hat{b}_n) + \lambda^2\}|n\rangle\langle n| + J_{coulomb} \cdot \{|1\rangle\langle 2| + |2\rangle\langle 1|\} - \frac{2\left(t_e^2+t_h^2\right)}{E_{CT}-E_{S1}} - \frac{2t_e t_h}{E_{CT}-E_{S1}}\{|1\rangle\langle 2| + |2\rangle\langle 1|\}, \qquad (1.3),$$

where t_e, t_h are the charge transfer integrals, $t_e = \langle A^-BC^+|\hat{h}|AB^-C^+\rangle \approx \langle l_A|\hat{h}|l_B\rangle, t_h = \langle A^+BC^-|\hat{h}|AB^+C^-\rangle \approx -\langle h_A|\hat{h}|h_B\rangle$, $\hat{h}$ is the single electron transfer Hamiltonian, l_A, l_B are the lowest unoccupied molecular orbital (LUMO) of the A and B sites, h_A, h_B are the highest occupied molecular orbital (HOMO) orbitals of the A and B sites, E_{CT} is higher-energy of CT exciton, and E_{s1} is the localized molecular excitation energy, $\hat{b}_n^+$is the creation operator of vibrational excitation, $\hat{b}_n$is the annihilation operator, $\hbar\omega_0$ is the vibrational excitation energy, and

$\lambda^2$is the Huang-Rhys factor.[11] The relative sign of t_e, t_h in last term coupling energy $-\frac{2t_e t_h}{E_{CT}-E_{S1}}$ determines whether a positive or negative coupling energy.[9]

Facilitated by the wave-function overlap, the charge transfer which creates an effective short-range exciton coupling that can also induce the J-or H aggregate behavior and is very sensitive

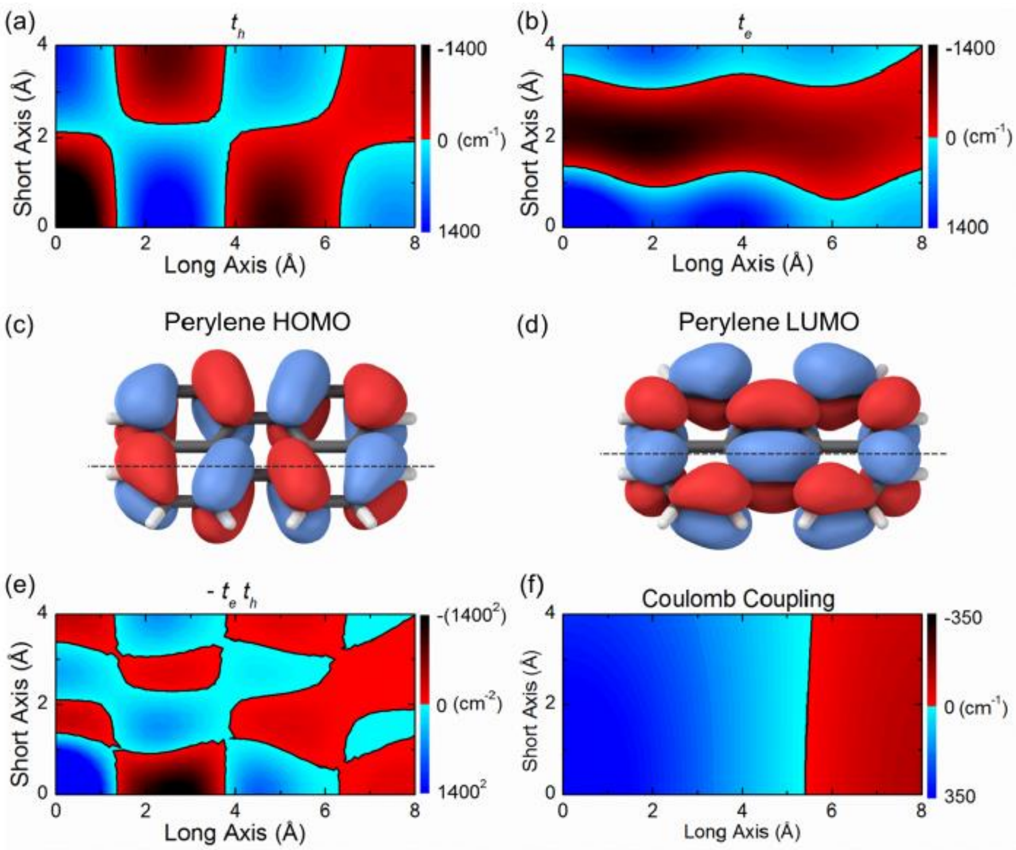

Figure 7. (a) t_h and (b) t_e within a π-stacked perylene dimer (3.5 Å π-stacking distance) as a function of transverse displacement, evaluated from the density functional theory (DFT) calculated energy level splittings. The DFT calculated (c) HOMO and (d) LUMO of perylene. (e) The product, $t_e t_h$ ($\propto J_{CT}$), and (f) the unscreened Coulomb coupling as a function of transverse displacement, evaluated using the time-dependent DFT calculated atomic transition charge densities. Red (blue) regions correspond to a J- (H-) type interaction. Adapted from Ref.7.

to the small (sub-Å) displacement between chromophores. Figure 7 shows the density functional theory (DFT) calculated charge transfer integrals and their product with respect to the chromophore displacement.[9] Small transverse displacement leads to the interconversion between H and J coupling in the charge transfer interactions, revealing extremely high sensitivity of the CT couplings in terms of the configurations of chromophores.[9]

On above all, the FE and CT couplings altogether determines the H and J spectral properties and are entangled in the spectra. The work function is the energy to promote an electron from Fermi level (electron chemical potential) to the vacuum level, plays a significant role in electronic and optoelectronic properties. For example, the work function in the interface in photovoltaic device significantly influences the open circuit voltage, and modification of the electrode work function can tune the charge injection/extraction.[12] Ubiquitous in the aggregates, disorders such as defects and dislocations directly influence not only the dipole orientations and displacement, impacting the FE couplings; but also the chromophore wave-function overlap, thus affecting the CT couplings.[2] However, knowledge about how the order influences the work function in organic semiconductor assemblies is still insufficient. Herein, we mainly focus on addressing the question how the ground state CT-interaction-perturbed work function is correlated with the order in organic semiconductor assemblies. I used the integrated KPFM and PL spectroscopy to link the work function with the π stacking order, and discovered as the π stacking order enhances, the work function in the organic semiconductor assemblies decreases.

1.2 Experimental Approach

The photoluminescence (PL) spectral signatures entangle both the “bright” (FE) and “dark” (CT) couplings, and the I_{00}/I_{01} intensity ratio encodes the structural information about the packing motif. Hestand and Spano had in-depth discussion and theoretical simulation in the paper “Interference between Coulombic and CT-mediated couplings in molecular

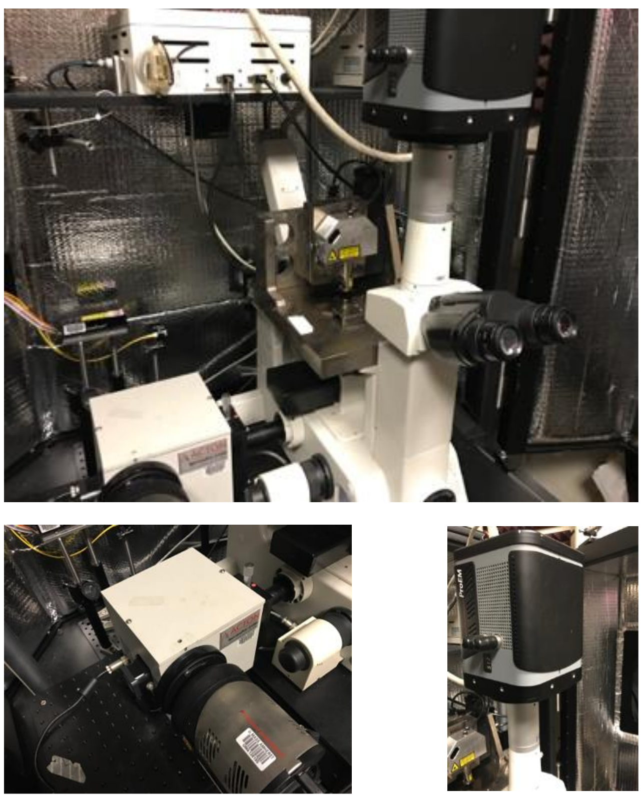

Figure 8. The apparatus of the combination of the scanning probe microscopy (TOP), the photoluminescence spectrograph (Lower-left) and the photoluminescence imaging camera (Lower-right) which are coupled to SPM.

aggregates: H to J-aggregate transformation in perylene-based π-stacks”.[13]

However, the “dark” couplings cannot be evaluated by the PL alone. With the purpose to disentangle the “bright” and the “dark” couplings, the Kelvin Probe Force Microscopy (KPFM) was integrated in concert with the PL spectroscopy in this research. Figure 8 shows the picture of the apparatus coupled by the KPFM, the PL imaging and the PL spectrograph.

The Kelvin Probe Force Microscopy (KPFM), integrated in the atomic force microscope (AFM),

is a scanning probe technique that has proven to be especially powerful in elucidating

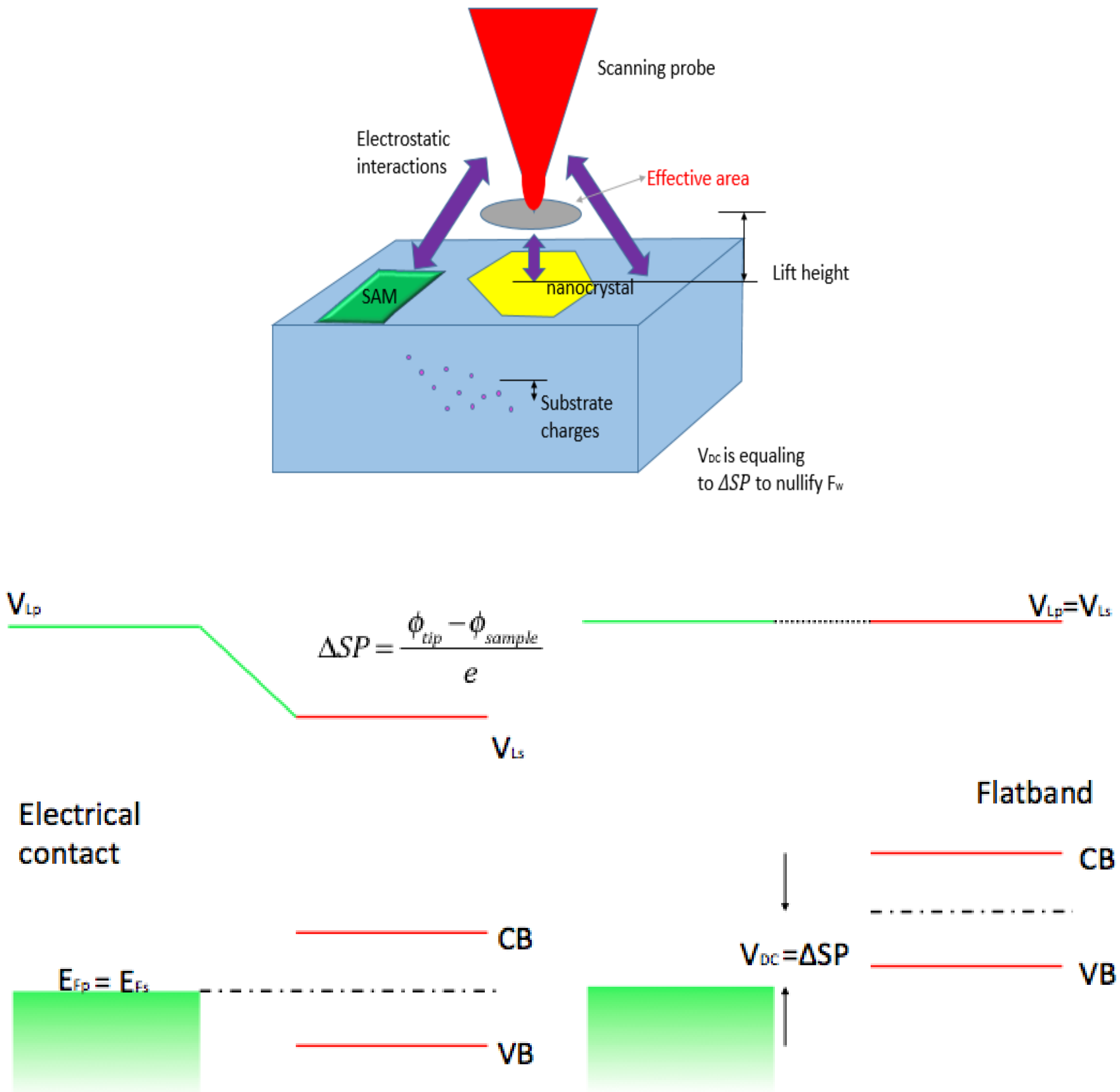

Figure 9. The schematic for the principle of the KPFM. The Top shows the electrostatic interaction between the scanning probe and the sample. The detection range of the KPFM is so-called effective area, determined by the nominal radius of the probe. The Bottom shows the energy band diagram of the electrical contact between the probe and the sample. The surface potential contrast results from the work function difference between the probe and the material. A DC voltage is applied to make the vacuum level flat band.

connections between the molecular packing morphology and the electronic properties. Baghgarbostanabad et al in our lab studied the correlation between molecular weight of P3HT and the surface potential contrast (SPC or ΔSP).[14] Palermo et al used the KPFM to find the work function change with the different-chain-length-oxysilane in various morphologies including the layers, the network of fibers, and the elongated agglomerates.[15] Figure 9 illustrates the configuration and the interaction between the scanning probe and the object. The KPFM exploits a capacitive interaction between a metallically-coated tip (typically Pt), and the material under investigation (Figure 9), with a lateral resolution defined by the tip radius (~20-30nm). The capacitive force between the tip and sample is

$$F_{es} = -\frac{1}{2}\Delta V^2 \frac{dC(z)}{dz}, \qquad (1.4).$$[16]

When a DC and AC mixed voltage is applied as: $\Delta V = V_{tip}$-$\Delta SP = V_{DC} - \Delta SP + V_{AC} sin\omega t$, where ΔSP is the work function difference of the tip and the sample. The results are composed of three components (a DC component, a single ω component and a double ω component):

DC component:

$$F_{DC} = -\frac{1}{2}\frac{dC(z)}{dz}(V_{DC} - \Delta SP)^2, \qquad (1.5)$$

single ω component:

$$F_{\omega} = -\frac{dC(z)}{dz}(V_{DC} - \Delta SP)V_{AC}sin\omega t \ , \tag{1.6}$$

double ω component:

$$F_{2\omega} = \frac{1}{4}\frac{dC(z)}{dz}V_{AC}^{2}[cos2\omega t - 1] \ , \tag{1.7}$$

where $\frac{dC(z)}{dz}$ is the z derivative of the capacitance between the probe and the sample.[15]

When a DC voltage equaling to the work function difference is applied, the single ω force is nullified (eq.1.6). If the tip work function is calibrated and through the single ω term (eq.1.6), the experimental value of work function of the sample is readily acquired. The energy resolution can reach an order of a few meV.

The principal advantage of the experimental approach illustrated in Figure 8 is that it is possible to do the scanning probe microscopy and also obtain the spatially-registered photoluminescence (PL) spectra. Figure 10 shows clearly the spatial coordinates of the AFM image and the PL image are registered, ensuring the spatial correspondence of the AFM and the PL measurement.

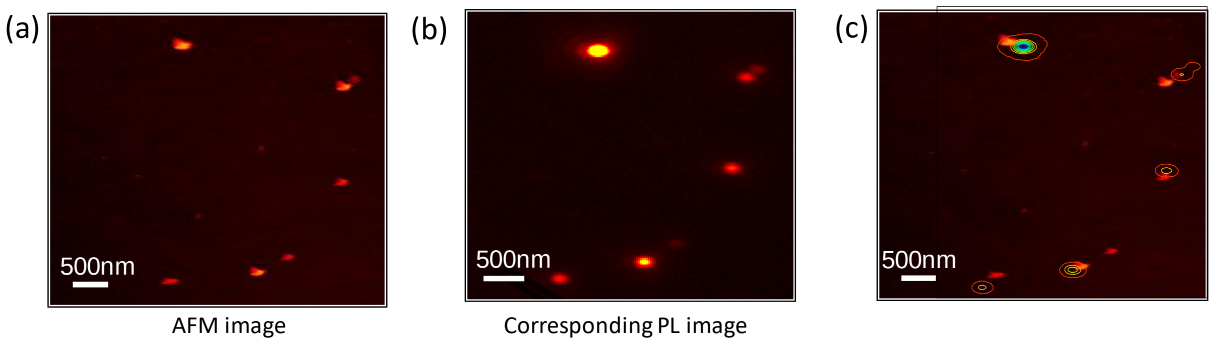

Figure 10. The registration of the AFM image and the PL image by the quantum dots. (a) the surface height image. (b) the PL image. (c) superposition of the AFM image and the contour plot of the PL image. Scale bar: 500nm.

Through the registration of the PL spectrograph and the KPFM, we are able to acquire in-situ spectra after obtaining the KPFM image. Although the PL entangles both the “bright” and the “dark” couplings, the work function is only influenced by the “dark” couplings. Figure 11 shows the energy levels, resulted from the ground state CT couplings: The valence band maximum (VBM) is lifted up by $2|\langle t_h \rangle|$ during aggregation of the

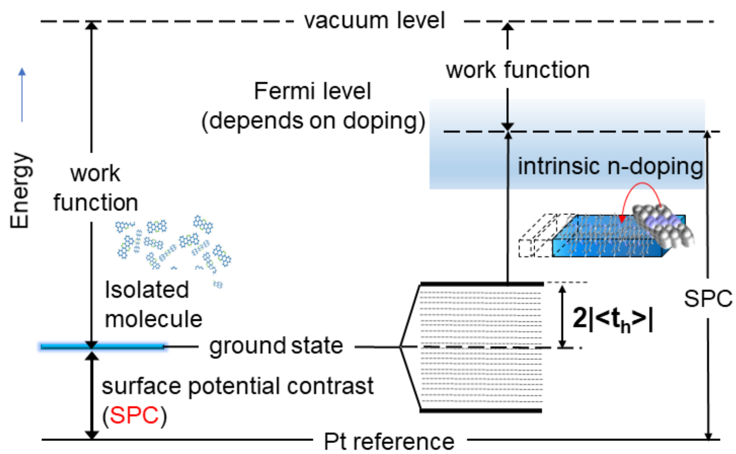

Figure 11. The energy level diagram for the TAT system in the transition from isolated (uncoupled) molecule to crystalline aggregate. The valence band maximum is raised by the magnitude of $2|\langle t_h \rangle|$. Note that the SPC is measured relative to the Pt reference.

organic semiconductor molecules, manifested as an elevated SPC. Thus, we can evaluate the CT coupling-perturbed work function and are pointed to a route to disentangle the “bright” and the “dark” couplings, combined with the structural information (both the FE and CT) encoded in the spatially- registered PL spectra.

The materials platform we selected is the 7,8,15,16-tetraazaterrylene (TAT). Figure 12 shows the spatial arrangement and the molecular structure of TAT.[11] TAT is a suitable material platform due to: First, TAT aggregates are highly photostable, and its vibronic structure is preserved upon aggregation where the intensity profile encodes the information on the packing structure and the pi-stacking order.[17]

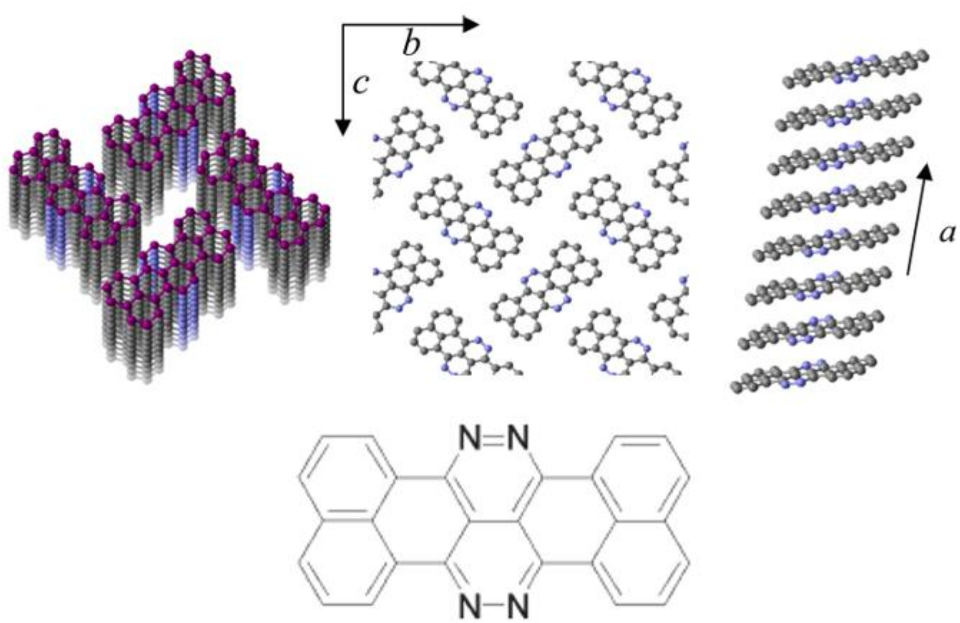

Figure 12. The spatial arrangement of TAT in bc plane and a axis. The bc plane displays a spiral arrangement, while TAT π stacks along a axis (Top). The molecular structure of TAT (Bottom).

Second, both long-range Coulombic couplings and short-range Charge Transfer (CT) couplings exist in TAT. Third, TAT aggregates have been studied extensively theoretically, the simulated spectra were established, and both the FE and the CT coupling matrix elements have been computed, providing a quantitative basis for experimental comparison with theory.[11] Fourth, the spiral arrangement minimizes the intra-plane couplings, leaving only couplings along the π stacking axis (Figure 12 Top), providing a platform convenient to exclude other disturbing influences.

1.3 Results and discussions

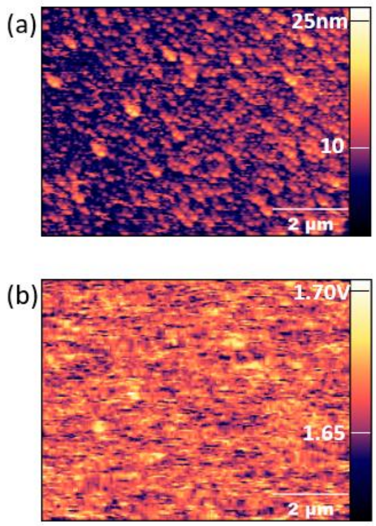

Figure 13. The surface height (a) and the SPC (b) images of the spun-cast TAT film. Scalebar: 2um. Through the height image, randomness of the spun-cast TAT stacking was revealed.

Various morphologies of the TAT including the spun-cast TAT film, the TAT nanowires, the nanowire bundles and the TAT nanoclusters were investigated to see how pi-stacking order affects the work function. Figure 13 displays the surface height and the SPC images of the spun-cast TAT film, exhibiting the disorder of stacking. The randomness of orientations minimizes the coupling, leading to a total zero CT integral, confirmed by the spectrum of the spun-cast TAT also showing a PL spectrum with vibronic intensity ratio (00/01) of 1.4 (Figure 17B top spectrum), resembling the uncoupled TAT in the dilute TAT solution and those of single TAT molecules assayed in polymer-supported thin films. Figure 14

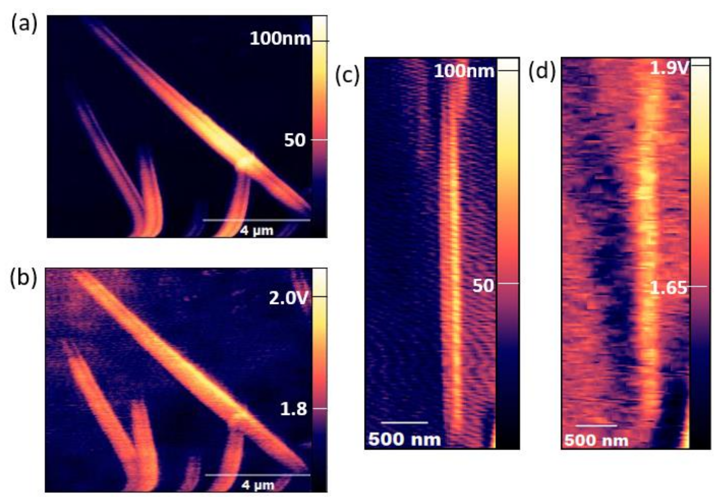

Figure 14. The surface height (a) and the SPC (b) images of TAT nanowire bundles. Scalebar:4um. The surface height (c) and the SPC (d) images of isolated thin nanowires. Scalebar:500nm.

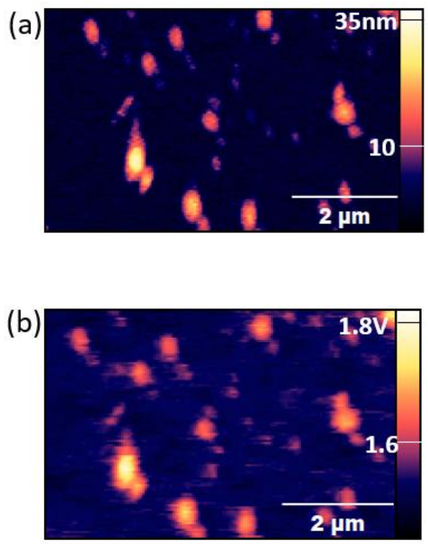

Figure 15. The surface height (a) and the SPC (b) images of TAT nanoclusters. Scalebar:2um. Some finer structures were seen in between the nanoclusters.

shows the surface height and the SPC images of TAT nanowire bundles and isolated thin nanowires prepared by recrystallization by drop-casting TAT/chloroform solution on glass slide. Figure 15 shows the surface height and the SPC images of TAT nanoclusters. In between nanoclusters, finer structures can be found. The SPC images (Figure 13b, Figure 14b, d and Figure 15b) show that the nanowires and nanoclusters have an SPC higher than that of spun-cast TAT film. Figure 16A, B exhibit the TEM images and diffractions of the TAT nanowire bundle

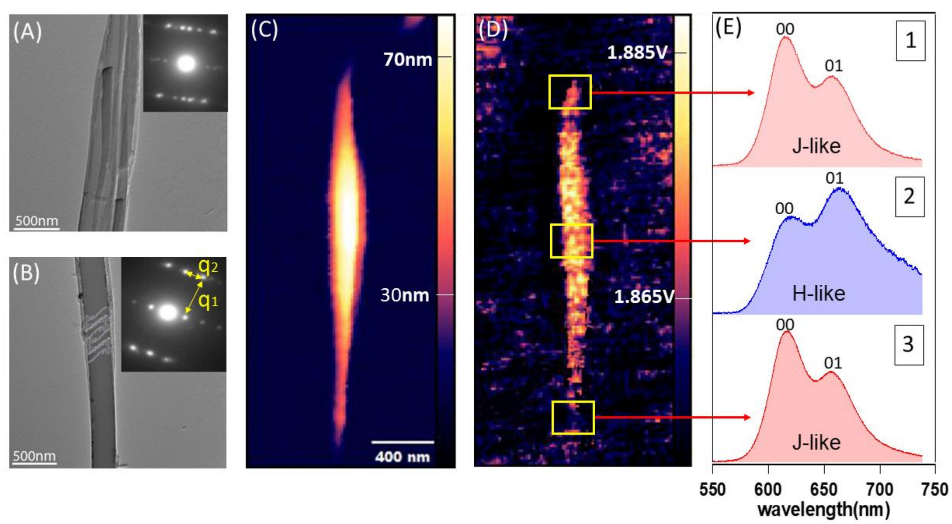

Figure 16. (A, B) The TEM images and the diffraction patterns (insets) of TAT nanowire bundles and isolated wires prepared by self-assembly from the toluene solution. The wires show characteristic reflections (q1, q2) of a monoclinic unit cell with real space distances of 3.9 Å, and 9.6 Å associated with the crystallographic **a** and **b-c**, directions respectively.[1] (C, D) The surface height and the SPC image of an isolated TAT nanowire, along with (E) the axially resolved PL spectra obtained from the either end and middle. The spectra clearly indicate different packing motifs at the nanowire ends which induces spectra closer to disordered TAT. The spectral types and the peaks are labeled.

and the single crystalline nanowire. The axially resolved spectra are acquired along the nanowire, showing that the two ends display

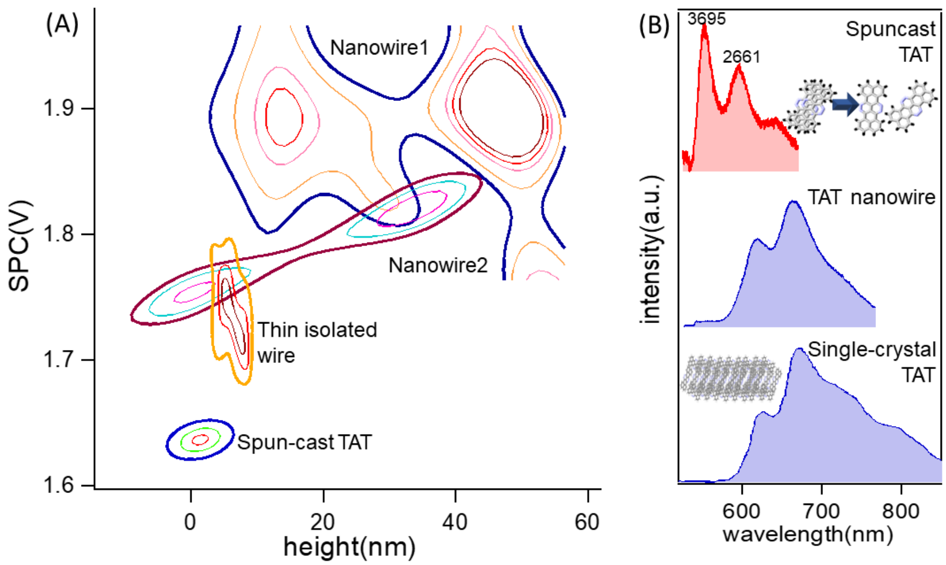

Figure 17. (A) The contour plots of the SPC vs. the sample height comparing the spun-cast TAT thin film, the isolated nanowire, and different nanowire bundles. (B) Representative PL spectra of the spun-cast TAT, the nanowire, and the single-crystal TAT (The spectrum of single crystal TAT is adapted from Ref. 16).

a J spectral signatures, and the middle part shows an H spectral signature, indicating the ends are more disordered than the middle part (Figure 16E). Figure 17A shows the contour plots for SPC versus the height for the spun-cast TAT, the TAT nanowire bundles, the thin isolated nanowire. A decreasing trend of SPC with respect to the order and a weak dependence of the SPC on the size are demonstrated here. Figure 17B shows the spectral signatures of the spun-cast TAT, the TAT nanowire and the single crystal TAT. The TAT nanowire spectrum is very close to that of the single crystal TAT by physical vapor transport (PVT) despite some minor side features.[17] In Figure 17A, the mean SPC for the thin isolated wire is 1.72V, while different

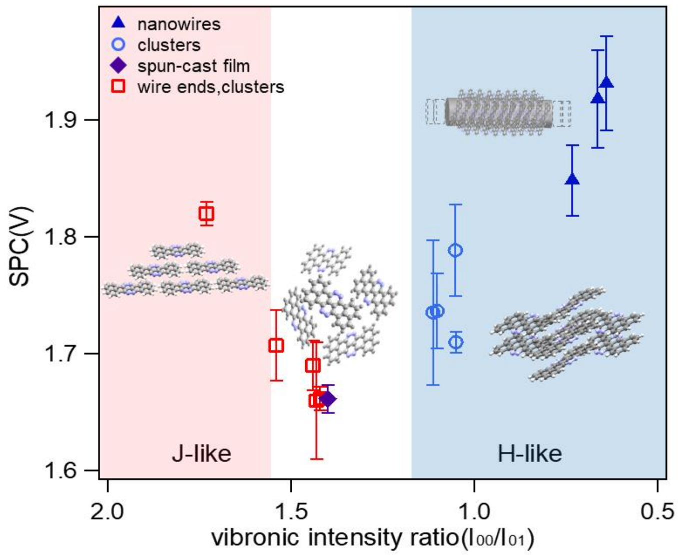

Figure 18. The correlation of the average SPC versus the vibronic intensity ratio for various TAT morphologies, including spun-cast TAT, nanowires, and both H-like and J-like nanoclusters. The color shading indicates H-like (blue) and J-like (red) spectral signatures. The similar SPC for both cluster types suggests a similar VBM rise for the J- and H-like clusters with just flipped HOMO top.

representative nanowire bundles show higher average SPCs (increased Fermi level) that are correlated with the surface height. The SPC upshift (the work function decreases) by approximately 110meV, in the thin TAT nanowires relative to the disordered spun-cast film, is in good agreement with the theoretically computed value of $2|\langle t_h \rangle| \approx 120$ meV.[11] Figure 18 displays the correlation of the average SPCs versus the vibronic intensity ratios I_{00}/I_{01} for various TAT morphologies. The spun-cast film shows the lowest SPC. In the H-like regime, the SPC increases, indicating a more or less monotonic work function decrease as the π stack order increases, signaled by decreasing vibronic intensity ratio. In the J-like regime, the SPC also increases, which we attribute to that the HOMO top only relates to the magnitude of t_h, but not the sign. When the sign of t_h changes, the split levels just flip. The filled HOMO band top still enhances. Thus, the SPC still sees an elevation.

The enhancement of the SPC from the thin wire to the nanowire bundles observes a weak size (volume) dependence. It is highly likely due to the effect of intrinsic n-doping of nitrogen substitution on the "shoulder" positions. This "intrinsic doping", when size-volume and carrier delocalization increases, further lifts the Fermi level and increases the energy difference between Fermi level and valence band maximum (VBM). Considering the structural similarity of oligoacene the TAT and the pentacene and the fact that the physical parameters are fully established for the model organic semiconductor pentacene, an estimate of the energy shift, ΔE, from the VBM to the Fermi level (see Fig. 11) is carried out to evaluate the effect of the intrinsic doping. By the carrier density formula from semiconductor physics,

$$p = N_V \cdot \exp[\frac{-\Delta E}{k_B\, T}], \qquad (1.8),$$

here N_v is the effective density of states, given by $2(2m^* k_B T/h^2)^{3/2}$, with m^* as the effective carrier mass, k_B is the Boltzmann's constant, h is Planck's constant, and T is the absolute temperature. Using values adopted from literature, in which $m^* \approx 4\ m_e$, N_V is $\approx 2 \times 10^{20}$ cm^{-3} at T = 300 K.[18] and number of holes, by Kobayashi and coworkers, $p = 3.25 \times 10^{16}$ cm^{-3},[19] an energy shift is estimated, $\Delta E \approx 230$ meV, which is close to the SPC upshift between the thin nanowire, and the nanowire bundles. In Figure 11 which illustrates the energy band diagram of the ground state interactions, a beautiful and elegant physical picture is depicted. During aggregation of the molecules, the ground state interactions split the HOMO level and form a band. The intrinsic doping effect further lifts the Fermi level and diminishes the work function, manifested as an enhanced SPC.

1.4 Summary

Through the spatially registered PL and the KPFM imaging, we found that the increase of π stacking order decreases the work function, resulting from the ground state CT-couplings, and revealed quantitatively the magnitude of CT-couplings, close to the theoretically computed value. The further upshift of the Fermi level, we believe is due to the intrinsic doping effect. This study is seminal for the future investigation in other organic semiconductors about correlation between the π stacking and the work function. It is possible to tailor the packing motif to engineer the coupling energy of the CT and the FE, thus the total coupling energy, to modulate the optoelectronic properties of organic semiconductors like the exciton coherence length. Since work function in organic semiconductor governs the charge injection/extraction in interfaces and the harvestable photovoltage directly, it is conducive to the work function engineering and functionalization of organic semiconductors toward the goal of tailoring the packing motifs to enhance the directional charge/energy transport.

CHAPTER 2

WORK FUNCTION TUNING OF MoS_2 BY NON-COVALENT CHEMICAL DOPING

2.1 Introduction and Overview of the second project

Transition Metal Dichalcogenides (TMDC), such as MoS_2, are two-dimensional materials like graphene, possessing both electron (n-type) and hole (p-type) conduction characteristics.[20-22]

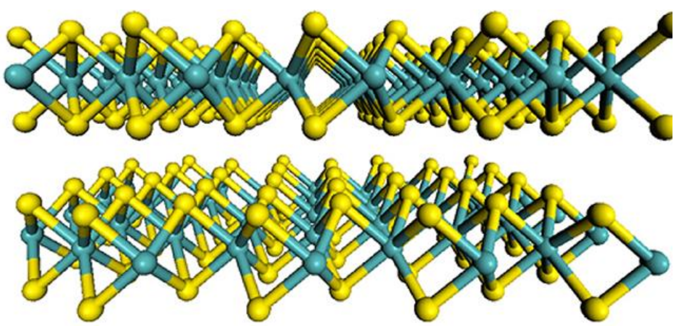

Figure 19. The MoS_2 ball and stick structure. Cyan balls represent the Molybdenum atoms, yellow balls represent the Sulphur atoms.

The structure consists of molybdenum atoms sandwiched between two layers of sulfur atoms, forming a two-dimensional monolayer. Figure 19 shows the ball and stick representation of an MoS_2 lattice. The distortion of the relative position of the Molybdenum and Sulphur atoms results in two different crystal symmetries: 1T metallic phase and 2H semiconducting phase, exhibiting a conductivity tunability. MoS_2 possesses excellent electronic properties, for example, monolayer MoS_2 displays a high electron mobility (~200 $cm^2 V^{-1} s^{-1}$)[23] and large current on/off ratios (~10^8).[23-24] Along with ambipolar charge conduction

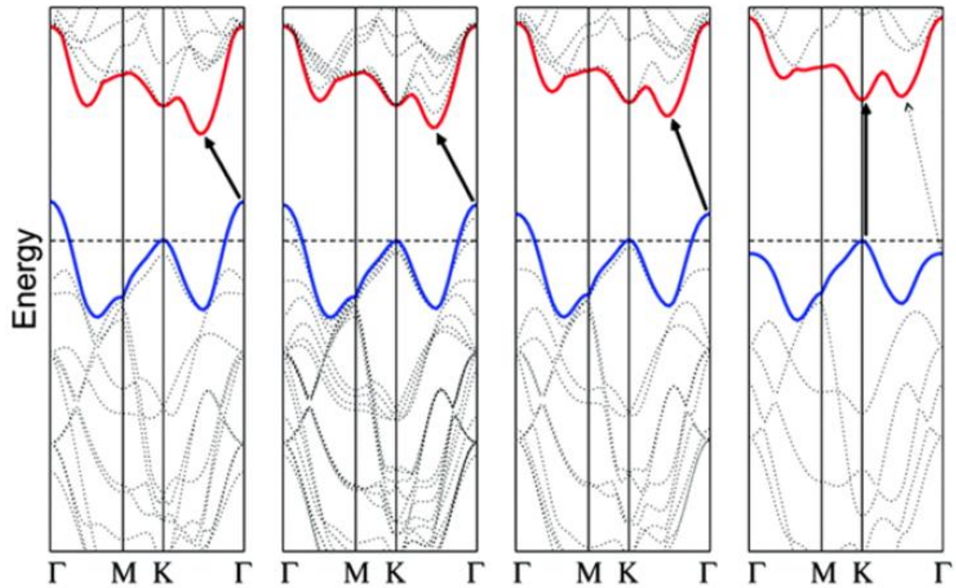

Figure 20. (Left to Right) Energy band structures of bulk, trilayer, bilayer and monolayer MoS_2 calculated by the density functional theory (DFT), showing the increase in band gap and the transition from indirect band gap of the bulk to direct band gap for the monolayer MoS_2. Adapted from Ref.5

characteristics, unlike graphene which is semi-metallic, semiconducting MoS_2 exhibits an inherent, layer-dependent bandgap, transitioning from an indirect bandgap of 1.2 eV to a direct bandgap of 1.8 eV at monolayer thickness. The presence of a bandgap is favorable for electronics applications and is a promising candidate in the next-generation devices .[24] The evolution of the bandgap with layer number is shown in Figure 20 using density functional theory calculations (DFT). In order to implement TMDCs in devices, the work function must be taken into consideration as it directly determines device properties. For example, in diodes of TMDC and another material, the difference of the work function in p and n sides determines the potential barrier in the junction, bends the energy band structure, and governs the direction of charge flows; if the TMDC is used as an electrode in photovoltaic devices, the work function of the electrodes and n-materials determine the open-circuit voltage.[16, 25] Therefore, a convenient route to tune the work function will benefit the device engineering of MoS_2 and expand the utility.

Methods to tune the work function of MoS_2, like mechanical strain, heterostructure fabrication, or transition metal substrates have been demonstrated.[26-28] Lanzillo *et al.* reported DFT simulations using the strain to tune the work function, and showed compressive strain decreases the work function while tensile strain may initially increase the work function but ultimately decrease the work function.[26] Feng Li *et al.* reported the work function decreases for the MoS_2 on Pt substrates.[27] Qiang Zhang *et al.* fabricated hBN (hexagonal boron nitride) on the transition metal Ru to form a Van der Waals heterostructure-substrate to decrease the work function, due to the strong interaction between hBN/Ru.[28] While these methods changed work functions, they typically involve ultra-high vacuum deposition or use of transition metal substrates which are not scalable and expensive. Dongming Sim *et al.* showed work function change under chemical modification by thiol-group, but it irreversibly altered both the physical and electronic structure of MoS_2 and also the covalent chemical doping calls for vacancies which can influence the charge transport properties.[29] On the other hand, non-covalent functionalization of the basal plane of

2D materials, will circumvent problems that conventional methods present, like the requirement of ultrahigh vacuum or unscalable transition metal substrates. Besides, non-covalent chemical doping also provides an approach to integrate with lithography to realize spatial patterning and modulation of the electronic characteristics of the material that the covalent doping method is not capable of.[30] We wanted to address the question how non-covalent chemical doping tunes the work function of MoS_2 in this research. In this investigation, I used organic n- and p-dopants, in collaboration with the Emrick group in the Polymer Science and Engineering at UMass Amherst, to bidirectionally tune the work function of MoS_2 by non-covalent chemical doping.

2.2 Experimental Approach

The combination of the KPFM and the spectroscopy is a powerful tool to monitor work function changes in TMDCs. The KPFM allows measurement beyond just the contacting interfaces; previous research shows that it possesses a penetration depth ~ 100 nm in organic semiconductors[31-33] such that the KPFM can interrogate the Fermi level and the work function in MoS_2 below the layer of organic coating. Furthermore, the Raman spectroscopy encodes the structural information of MoS_2 such as the in-plane and the out-of-plane stretching, manifested as E_{2g}, A_{1g} peaks.[27, 34] The energy separation between these two peaks varies when layer number changes, acting as an indicator of the layer number.[34] Monolayer MoS_2 also possesses characteristic peaks in the PL spectrum, specifically a major “A” peak at around 660 nm, and a minor “B” peak at around 620 nm.[35-36] The intensity of PL peaks diminishes around three to four times as the layer number increases from monolayer to three or four layers, due to the rotational stacking disorder and transition from indirect bandgap to direct bandgap.[37] Therefore, combination of the KPFM and the spectroscopy offers a technique route to study the work function tuning of MoS_2, and also determine its layer number.

2.3 Results and discussions

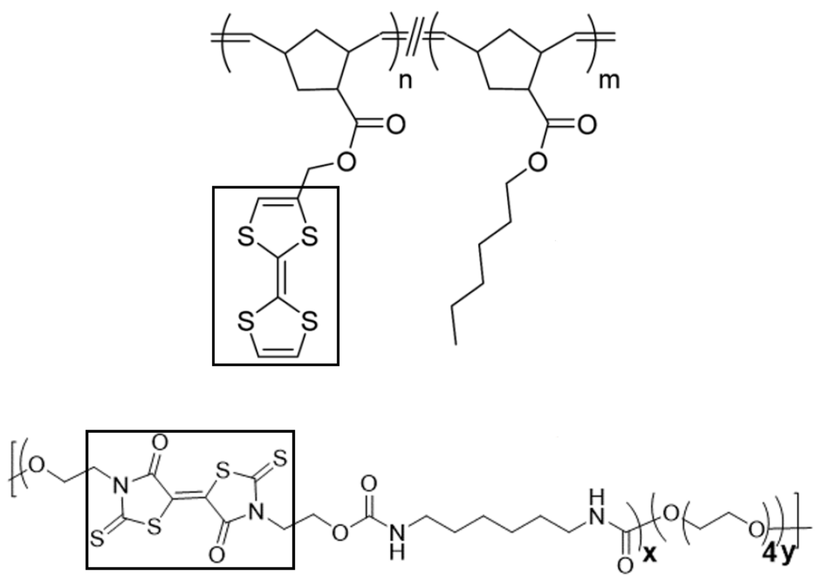

Figure 21. (Top) The TTF-contained polymer PolyTTFNB-50. The black box shows the TTF part. (Bottom) BT-contained polymer. The black box shows the BT part. The number in the compound title for PolyTTFNB-50 denotes the mole-percent incorporation of the TTF-containing repeat units.

We used electron donating tetrathiafulvalene (TTF) and accepting bithiazolidinylidene (BT)-containing polymers, synthesized by the Emrick group, for initial chemical doping studies. Both functional donor and acceptor components are sulfur-rich with the intention to promote adhesion to the MoS_2 through sulfur-sulfur interactions. The molecular structures of these polymers are shown in Figure 21.

Ramasubramaniam and coworkers conducted density functional theory simulations on the work

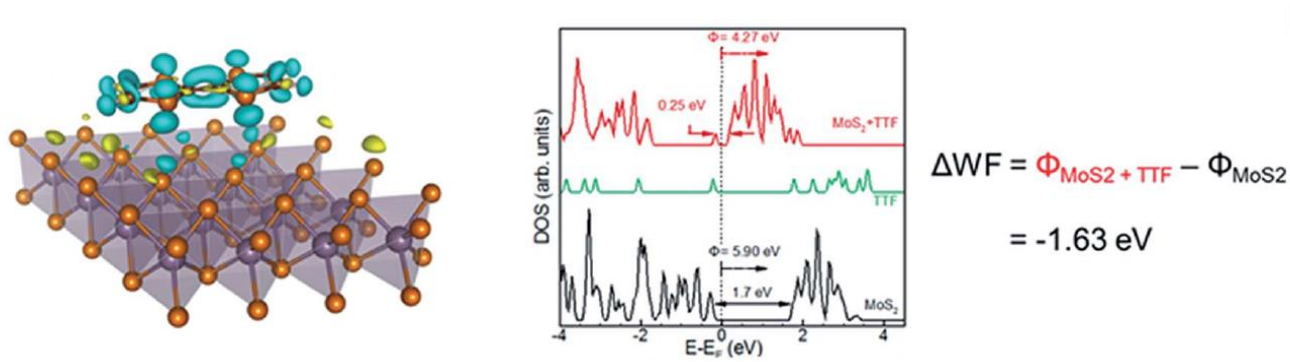

Figure 22. DFT computations for a single TTF molecule adsorption on the MoS_2. (Left) Charge density difference. (Right) Density of states plots. The results reveal a work function change of 1.63eV after doping TTF.

function modulation of MoS_2 by physisorption of TTF (Figure 22).[38] Their simulations show a

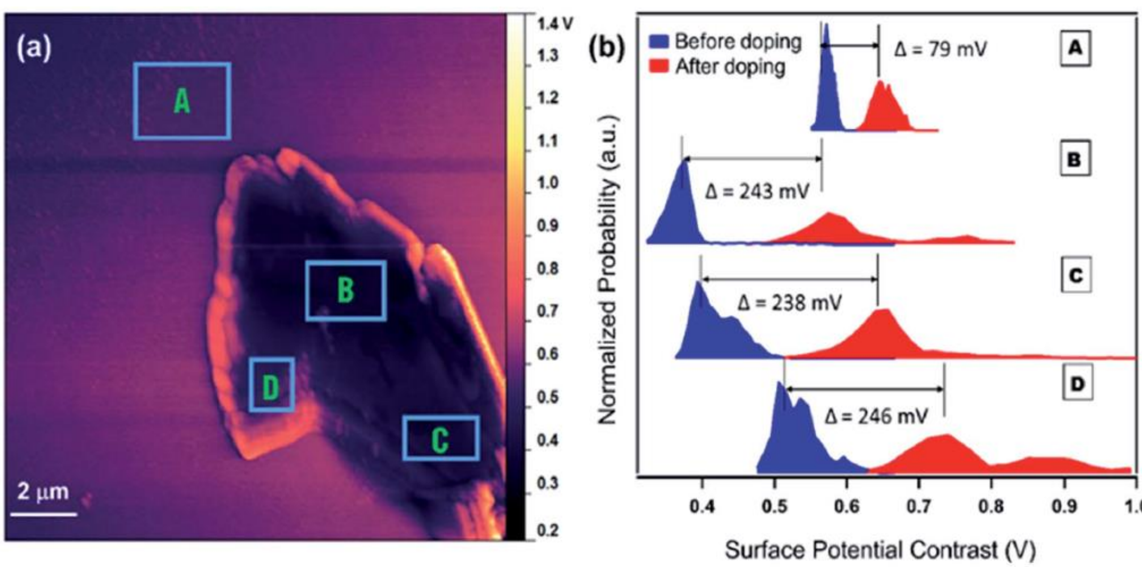

Figure 23. The KPFM scan on MoS_2 flake. (a) the SPC image of an MoS_2 flake prior to doping. (b) Normalized histograms of the SPC values in selected regions of interests before (blue) and after (red) doping with the polyTTFNB-50 (0.001mg/mL solution in THF). Region “A” shows the effect of polymer only (~5nm thickness) on the glass.

work function change by as much as 1.63 eV when TTF is adsorbed to the basal plane of

single-layer MoS_2 as the density of states (DOS) of the conduction band shift to the Fermi level

(Figure 22 Right). The conduction band becomes closer to Fermi level after doping the TTF, implicating the increase of electron density i.e. n-doping of the TTF. To experimentally determine the work function changes of MoS_2 upon doping the polymer polyTTFNB-50 (Figure 21 Top) (0.001 mg/mL solution in tetrahydrofuran) to a chemically exfoliated MoS_2 on the glass. Figure 23a shows the KPFM images of the MoS_2 morphology after doping the polyTTFNB-50 and the resultant SPC shifts before and after application of the TTF polymer in the regions of interests labeled in Figure 17a. The MoS_2 regimes see a consistent SPC upshift (~ 240 meV), signifying a decrease in work function. A control region containing only polymer on the glass surface shows an SPC change of 79 meV. To study SPC changes associated with the MoS_2 thickness, we used the photoluminescence spectroscopy (PL). Figure 24 shows the SPC change in regions of interests

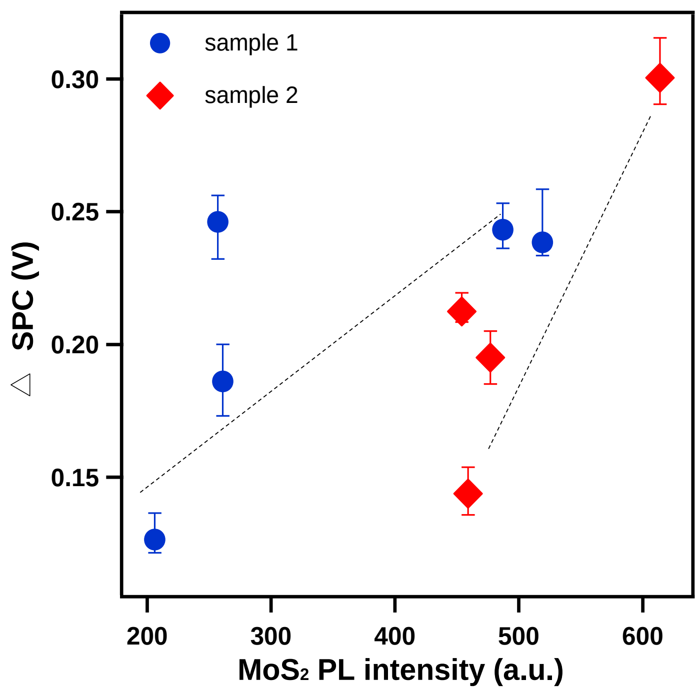

Figure 24. The correlation between the SPC and the PL intensity with same exposure time 2.5s from different regions of interests.

as a function of PL intensity; As the PL intensity increases, indicating a decrease in the layer thickness of MoS_2, the magnitude SPC upshift increases, displaying a thickness sensitivity. Multiple layer MoS_2 partitioned away the transferred carriers, diminishing the effect in shifting the Fermi level. While n-doping was observed for TTF adsorbed on MoS_2, the work function change is far smaller than the simulated results. We suspect this is due to the polymer backbone sterically hindering the contact between the TTF and the MoS_2 and a dilution effect occurring, when the layer number of MoS_2 increased beyond single layer. Using small molecule dopants on monolayer MoS_2 circumvents above possible problems and will be presented later.

Currently, there have been multiple literature examples of electron donating materials that decrease the work function of MoS_2 (n-doping),[29, 38-39] while electron acceptors (p-doping) that increases the work function of MoS_2 are not so many. However, device engineering such as p-n junction calls for full tunability of n-and p- doping. Therefore, we also carried out the p-doping experiments, using the BT containing polymer polyurethanes (BT-PU-25, 25 mol% BT) provided by the Emrick group. Figure 25 shows the surface height and the KPFM images of the BTPU spun-cast onto the single layer MoS_2 grown on sapphire (purchased from Sixcarbon Technologies). After dosing BT-PU-25, the height images reveal some agglomerations of the polymer forming, appearing as holes in the SPC image. In the histograms in the Figure 25 (Bottom), the SPC excluding those hole areas sees a 0.16 V downshift (work function increases) after coating the polymer, proving the p-doping of BT polymer. We still have doubt that the steric hindrance by the polymer backbone lowered the effect of p-

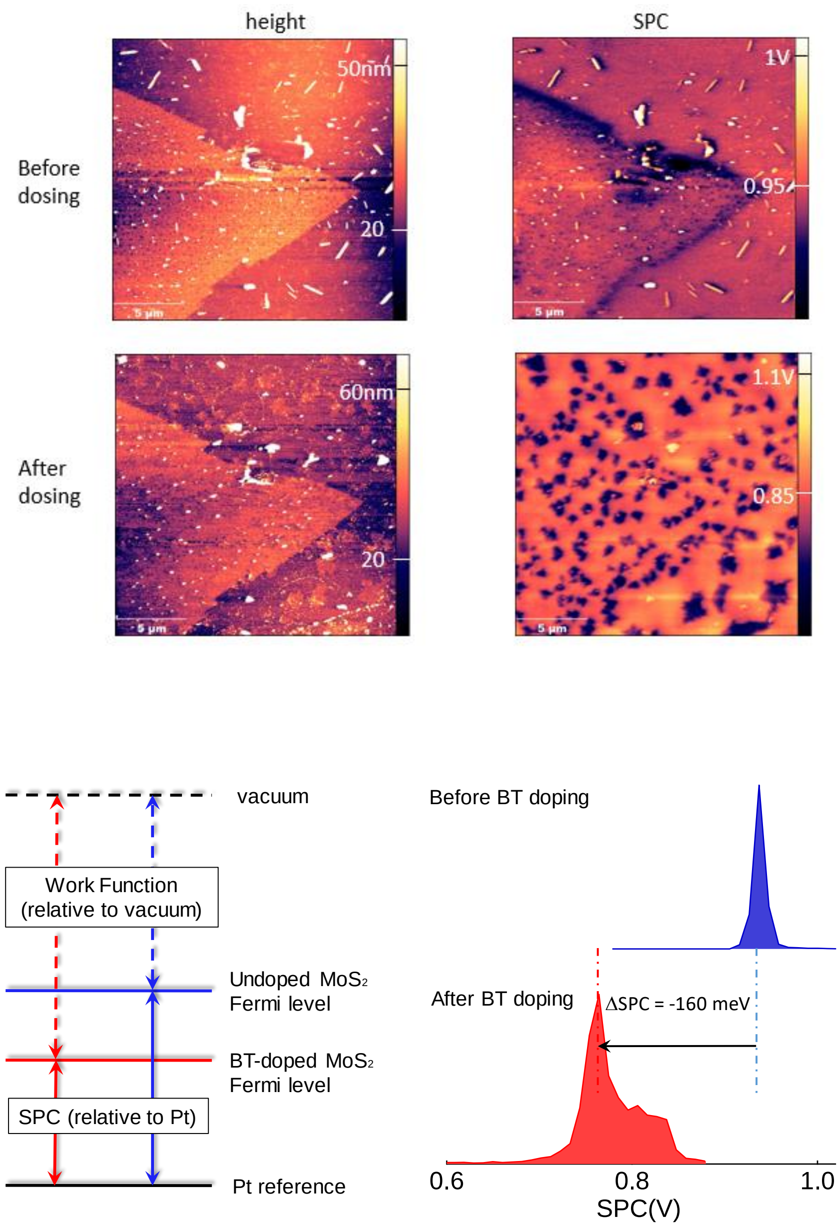

Figure 25. (Top) The surface height and the SPC image of the MoS_2 flake on sapphire before dosing the BT-PU-25. (Middle) The surface height and the SPC image of the MoS_2 flake after dosing the BT-PU-25. Scale bar: 5um. (Bottom) The SPC histograms before and after polymer coating. Data are extracted in the SPC image on MoS_2 excluding the holes which may be

doping by the BTPU, therefore the small molecule BT doping experiment were carried out and will be presented later.

To exclude the effect of the polymer backbone and the multiple layer MoS_2., we used the small molecules TTF and BT, and drop-cast dilute solutions directly onto the epitaxially grown MoS_2 (purchased from Sixcarbon Technologies).

The Raman and photoluminescence (PL) spectroscopy were performed on MoS_2 to assess the thickness. The Raman spectrum contains two characteristic transitions in the low frequency region: an in-plane (E_{2g}) and an out-of-plane (A_{1g}) stretch (Figure 26a). The peak distance between the E_{2g} and the A_{1g} within 20 cm^{-1} is a signature of the monolayer MoS_2.[27, 34] In Figure 26b, the PL peak at 660 nm is also indicative of the monolayer MoS_2.[36]

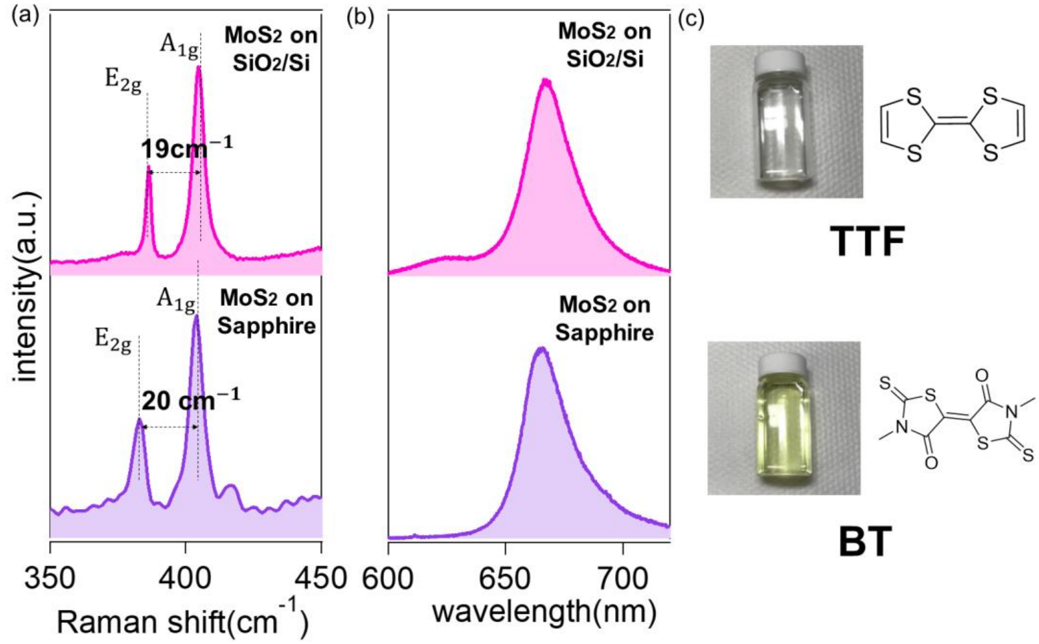

Figure 26. (a) The Raman spectra of MoS_2 on Si/SiO_2 (top) and sapphire (bottom) showing the in-plane and the out-of-plane stretches. b) The Photoluminescence spectra of MoS_2 on SiO_2/Si (top) and sapphire (bottom) showing the peak PL intensity at 660 nm, indicative of monolayer MoS_2. (c) Pictures of the TTF (n-dopant) and the methyl-BT (p-dopant) solution in the vials and the corresponding chemical structures.

Using n-dopant the TTF and p-dopants the methyl-bithiazolidinylidene (m-BT) and the butyl-bithiazolidinylidene (b-BT) we showed bidirectional work function tuning of MoS_2. Figure 27 exhibits the research theme and the striking work function shift achieved by the non-covalent chemical doping. The TTF displayed an SPC upshift in the Fermi level by 269 meV of the MoS_2 with underlying SiO_2/Si substrate, still smaller than the simulation value. We suspect that the substrate may play a role here and then purchased the CVD epitaxial MoS_2 on sapphire. The upshift of Fermi level of the MoS_2 on sapphire substrate is 1.24 eV, in much larger amplitude compared to the results in doping of the poly-TTFNB-50 and approaching the simulated results,

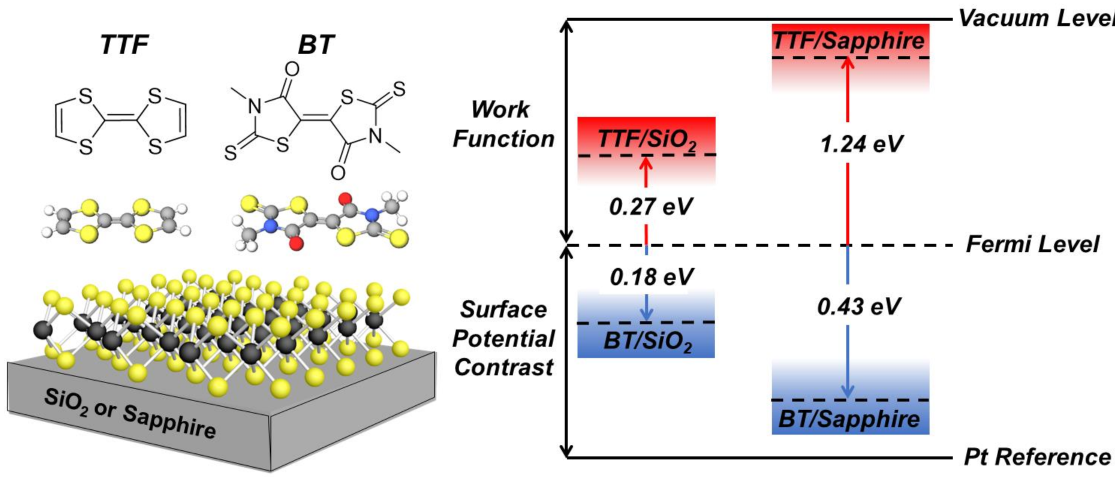

Figure 27. The summary of the KPFM study of bidirectional work function tuning of MoS_2 by non-covalent doping with different underlying substrates. The left portion shows the research theme. The right portion shows that the MoS_2 on sapphire possesses a larger work function change than the MoS_2 on SiO_2/Si after doping.

while the m-BT downshifting the Fermi level by 180 meV when the substrate is SiO_2/Si and downshifting the Fermi level by 434 meV with a sapphire substrate.

Figure 28, 29, 30 displays the surface height and the SPC images before and after drop-casting

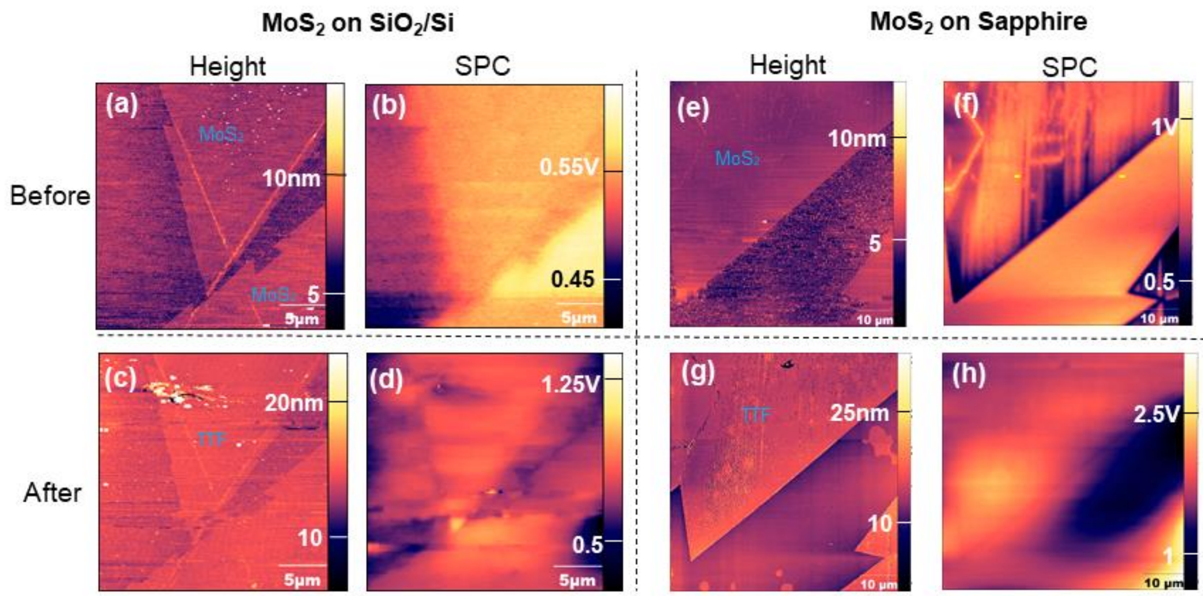

Figure 28. The surface height and the KPFM images of the TTF doping to monolayer MoS_2 with two kinds of underlying substrates. The MoS_2 on SiO_2/Si: Before doping the TTF: (a) surface height, (b) surface potential; After doping the TTF: (c) surface height, (d) surface potential, scale bar 5 um. The MoS_2 on Sapphire: Before doping the TTF: (e) surface height, (f) surface potential; After doping the TTF: (g) surface height, (h) surface potential, scale bar 10 um.

the dilute solution (0.005mg/mL in $CHCl_3$) of the TTF, the m-BT and the b-BT, respectively. The underlying substrates are either sapphire or SiO_2/Si. Work function calculated from Figure 29, 30 before doping is 5.1-5.2 eV, consistent with work function values reported in literature.[27, 38, 40] Figure 28a, c, display the morphology of MoS_2 on SiO_2/Si before and after doping the TTF. Upon addition of the TTF to MoS_2, the height histogram shifts indicate an 9 nm height change due to the organic layer (Figure 28a, 28c). Figure 31a summarizes the SPC shifts of the MoS_2 doped by the TTF, the m-BT and the b-BT by extracting the SPC values from the image pixels on the MoS_2 flake and displaying the SPC shifts as histograms. When the MoS_2 on SiO_2/Si was coated with the TTF, a 0.27 eV of upshift in the SPC was observed (Figure 28b, 28d, Figure 31a), corresponding to n-doping of the MoS_2, similar to our previous report using the TTF

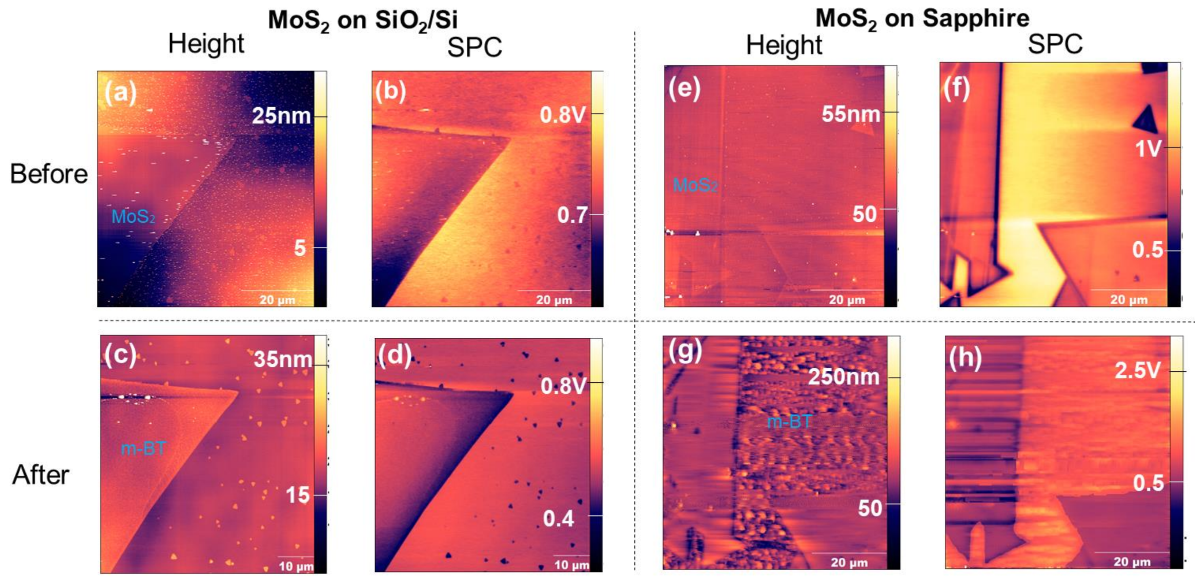

Figure 29. The surface height and the KPFM images of the m-BT doping to monolayer MoS_2 with two kinds of underlying substrates. The MoS_2 on SiO_2/Si: Before doping m-BT: (a) surface height, (b) surface potential; After doping the m-BT: (c) surface height, (d) surface potential, scale bar 10 um. The MoS_2 on Sapphire: Before doping the m-BT: (e) surface height, (f) surface potential; After doping the m-BT: (g) surface height, (h) surface potential, scale bar 20 um.

polymers.[38] However, when the sapphire was used as the underlying substrate (36 nm height shift from histogram analysis of Figure 28e, 28g), the magnitude of SPC upshift dramatically increased to 1.24 eV (Figure 31a), approaching theoretically predicted values (1.63 eV).[38] Reversed but similar patterns were observed in the SPC shifts of the MoS_2 coated with the m-BT and the b-BT. When the underlying substrate is SiO_2/Si, a 180 meV SPC downshift was seen for the m-BT with 7 nm height change (Figure 29a, b, c, d) and a 101 meV SPC downshift was observed for the b-BT with 4 nm height change (Figure 30a, b, c, d). Coating MoS_2 on a sapphire substrate with 36 nm thick layer of the m-BT (Figure 29e, g), showed a 434 meV downshift in the SPC. Coating MoS_2-sapphire with 2 nm b-BT organic layer showed a 237 meV downshift in

the SPC (Figure 31a). The SPC shifts are greater in the doping of the b-BT than the m-BT, which we suspect is due to the longer alkyl-chain hindering the contact between the BT and the MoS_2 basal plane.

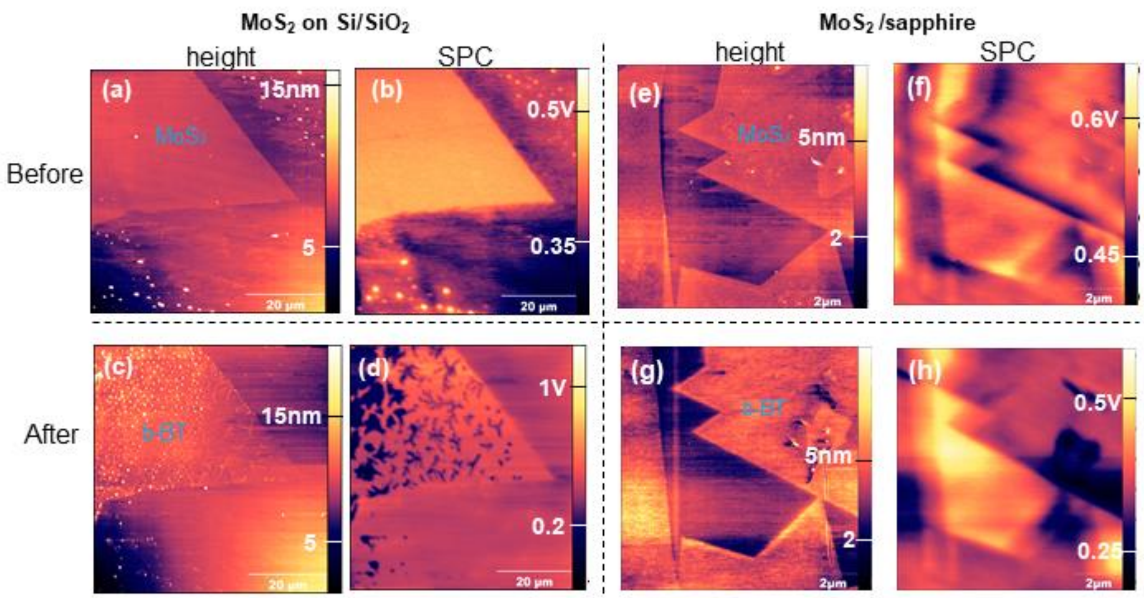

Figure 30. The surface height and the KPFM images of the b-BT doping to monolayer MoS_2 with two kinds of underlying substrates. The MoS_2 on SiO_2/Si: Before doping the b-BT: (a) surface height, (b) surface potential; After doping the b-BT: (c) surface height, (d) surface potential, scale bar 20 um. The MoS_2 on Sapphire: Before doping the b-BT: (e) surface height, (f) surface potential; After doping the b-BT: (g) surface height, (h) surface potential, scale bar 2 um.

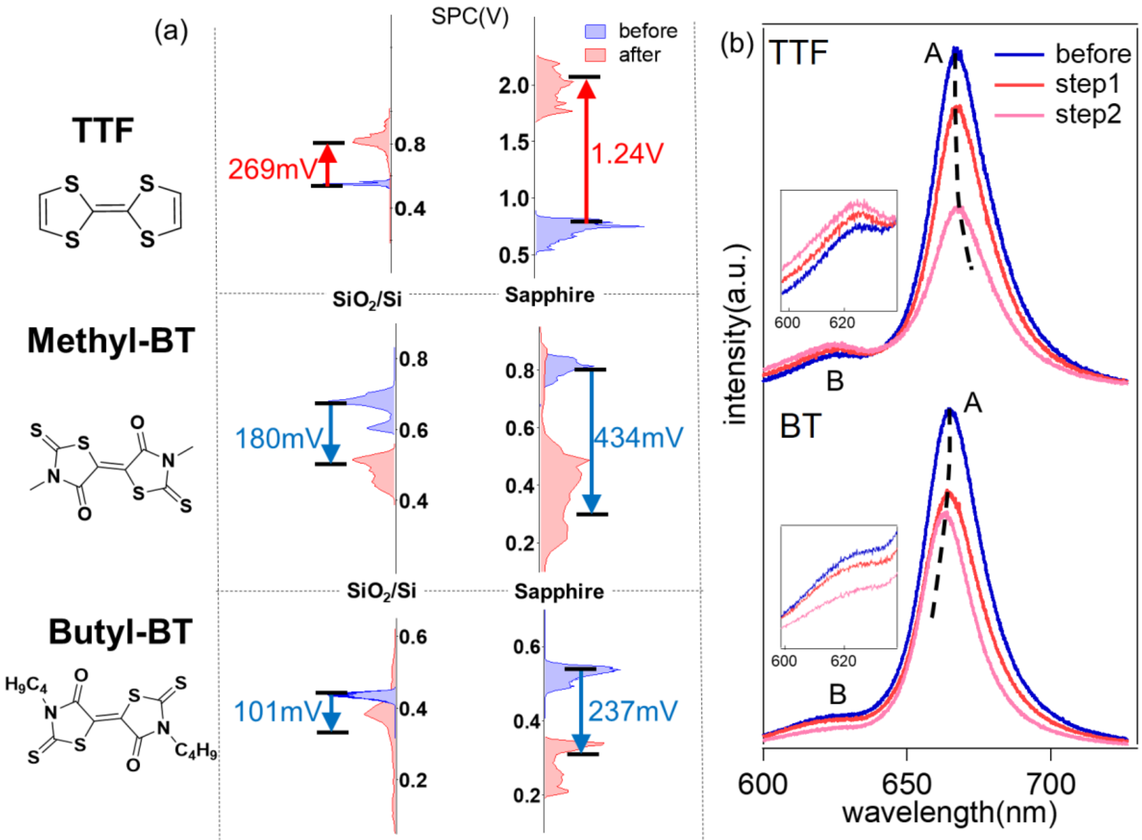

Figure 31. (a) A summary of the changes in the SPC of single layer MoS_2 before and after dosing the TTF, the m-BT and the b-BT on two substrates. The left portion shows the results of doping on SiO_2/Si, and the right portion shows the results from doping on sapphire. (b) the PL spectra of single layer MoS_2 on SiO_2/Si before drop-casting the dilute solutions of TTF and BT and after one and two additions of TTF and BT showing wavelength shifts corresponding to n- and p-doping, insets show the B peak of MoS_2.

In summary, after doping TTF, the SPC of the MoS_2 sees an upshift, indicating n-doping, while after doping the m-BT and the b-BT, the SPC sees a downshift, indicating p-doping. The MoS_2 both sees a symmetrically larger SPC change for both n- and p- doping on the substrate of the sapphire than the SiO_2/Si. To further confirm the n- and p-doping, I conducted the PL measurements before and after doping. Figure 31b shows the change of the PL spectra after doping the TTF and the BT: The PL spectra "red" shifts (4 nm) when doped with the TTF, indicative of n doping; and "blue" shift for 5 nm when doped with the m-BT, indicative of p-doping. The wavelength shift is due to the increase (n-doping) or the decrease (p-doping) of the charged exciton component which is at lower emission energy. Although the wavelength shift is consistent with literature reports,[36, 40] the intensity changes of the p doping are different from the increasing situation reported by a previous literature with a different kind of p-dopant,[36] which we believe is due to

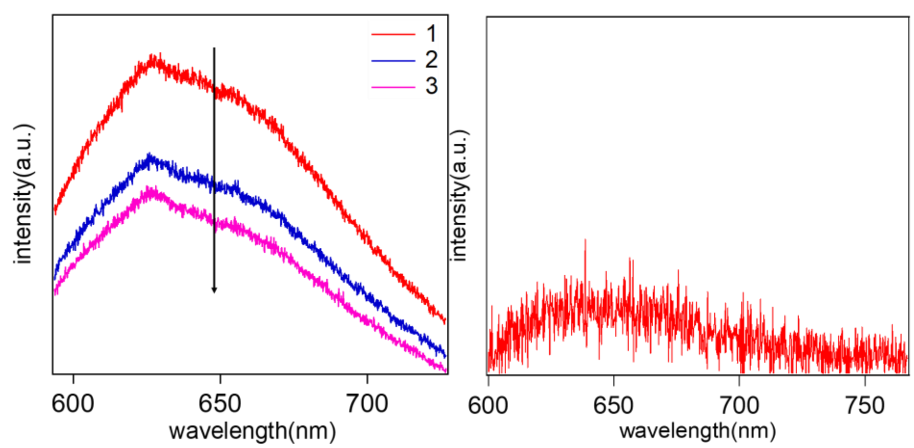

Figure 32. (Left) The photoluminescence spectra from the BT in the substrate background area in a two- step doping. 1, 2, 3 are taken continuously. (Right) The photoluminescence spectra from TTF in the substrate background area. The exposure time for both BT and TTF are 1s. The BT has an obvious absorption and photoluminescence, but the TTF has a very low photoluminescence. The scale of intensity for BT PL is 473-2431. The scale of intensity for TTF is 0-600.

photo-absorption, luminescence, and photo-decay of the BT, partitioning a portion of the excitation photons to BT over MoS_2. (Figure 32 shows the PL spectra of the BT and the TTF in background) and leading to the decrease of intensity in MoS_2.

The hypothesized reasoning for the substrate dependence is an induced static polarization at the interface between the MoS_2 and the substrates (Figure 33). The transfer of electrons between the TTF or the BT and the MoS_2 produces a dipole between the dopants and the MoS_2, pointing outwards respective to the MoS_2 for the former, and inwards for the latter. The former directionality decreases the work function and the latter directionality increases the work function.[41] The work function alteration can be estimated by

$$\Delta E_F = \frac{\sigma_d}{\varepsilon_0 \varepsilon}, \qquad (2.1),$$

where σ_d is the dipole moment area density, ε_0 is the vacuum dielectric constant, ε is the relative dielectric constant.[41] These charges generate induced static polarization which is just in opposite

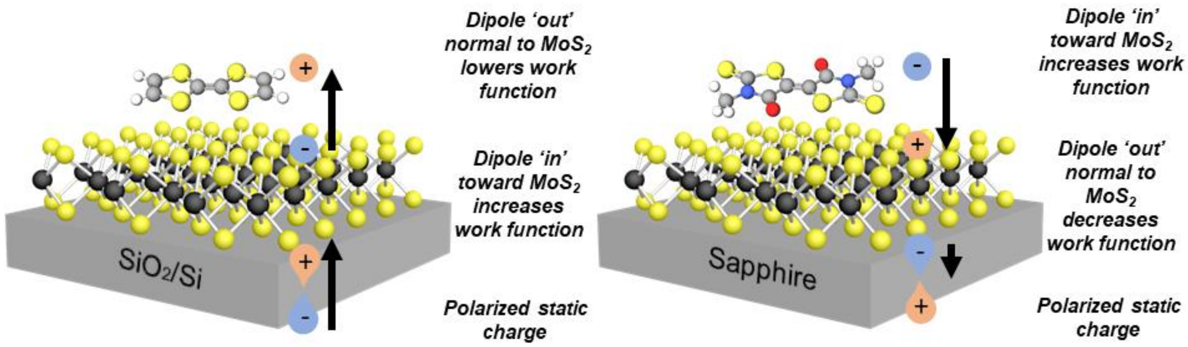

Figure 33. The physical picture of dipole and induced static polarization for the work function shift substrate dependence after doping (Left)the TTF, (Right) the BT. The transfer of electrons gives rise to dipoles between the dopants and the MoS_2 and the corresponding induced dipoles from the static charge at the dielectric/semiconductor interface. The dipole directs in toward MoS_2 increases the work function, the dipole directs out from MoS_2 lowers the work function. The final change of the work function results from the co-effect of the charge transfer dipoles and the induced static polarization.

directionality relative to MoS_2 at the substrate/semiconductor interface, effectively screening the measured surface potential. The opposite effect can also be calculated by eq.2.1. Increasing the dielectric constant reduces the magnitude of opposite offsetting. The sapphire possesses dielectric constant 3 to 4 times larger than that of SiO_2.[42-43] The opposite shift of work function is larger for the SiO_2/Si than the sapphire, leading to a diminished change in the measured work function.

2.4 Conclusion

In conclusion, we conducted n- and p-doping on the MoS_2 using the molecules that non-covalently adsorbed to the TMDC. The TTF upshifts the Fermi level and the BT downshifts the Fermi level in striking amounts. The substrates play a significant role in the work function shift. The sapphire substrate rather than the SiO_2/Si substrate observed a closer experimental value to the DFT simulation. We proposed a physical picture of co-effect of the charge transfer dipoles and the induced static polarization in the interface between the semiconductor and the substrate, offsetting the work function shift by the dopants. The BT with a longer side-alkyl-chain: butyl-group observed a smaller work function change than that of the methyl-group, potentially due to steric hinderance. Moreover, the TTF and BT containing polymer doping effect was also studied. The SPC change become less obvious due to the steric effects of the polymer backbone. Greater control over the work function of MoS_2 may now be exercised by selection of the non-covalently bound molecules and the substrates. This work points to a prospect of tailoring the MoS_2 work function over a wide range to achieve better suitability and versatility for electronics, introducing the potential for spatially-patterned MoS_2 electronics, and also guiding the rational design of MoS_2–based materials for device engineering in conjunction with high-level theoretical modeling efforts.

CHAPTER 3

INVESTIGATION OF THE SURFACE CHARGE AND POLARIZABILITY OF HETEROVALENT DOPED NANOCRYSTALS BY ELECTROSTATIC FORCE MICROSCOPY

3.1 Introduction and overview of the third project

Nanocrystals, usually in the size of tens of nanometers to several nanometers, possesses electronic properties differing strongly form their bulk counterparts, displaying discrete states and orbital shapes analogous to atoms and properties highly sensitive to quantum confinement effects.[44] The fact that the absorption and emission can be manipulated by tuning the bandgap, which is sensitive to the size, doping, structural or electronic defects and surrounding ligands, gives it an appealing prospect of the near-future application in smart windows, displays, biomarkers, and thus attract much attention from the scientific communities in the past twenty years.[45] For example, Granqvist et al. used WO_3/TiO_2 nanocrystals to make electrochromic smart windows which can change color adaptively to the daylight intensity and generate power.[46] Hetero-valent doped nanocrystals incorporate elemental impurities inside the host lattice, via a substitutional or interstitial doping mechanism which donates free carriers into the intrinsic nanocrystals and gives rise to unique electronic and optoelectronic properties such as catalysis and enhanced localized surface plasmon resonance (LSPR).[47] Figure 34 shows some example transmission electron microscope (TEM) images of Aluminum doped ZnO (AZO) hetero-valent nanocrystals under this investigation, displaying the scale of size of nanocrystals in this study. The surface charge of hetero-valent doped nanocrystals is closely connected with the luminescence dynamics like blinking.[48] A few of raw models were proposed concerning the charges in AZO, which have described the surface charge as arising from wavefunction expansion and the stabilization of interior carriers.[41, 49] Some researchers have suggested surface charges with some indirect evidences from time-resolved spectroscopy and transient absorption spectroscopy.[48, 50] However, direct experimental investigation about the charge in nanocrystals is lacking. The research question I focused on

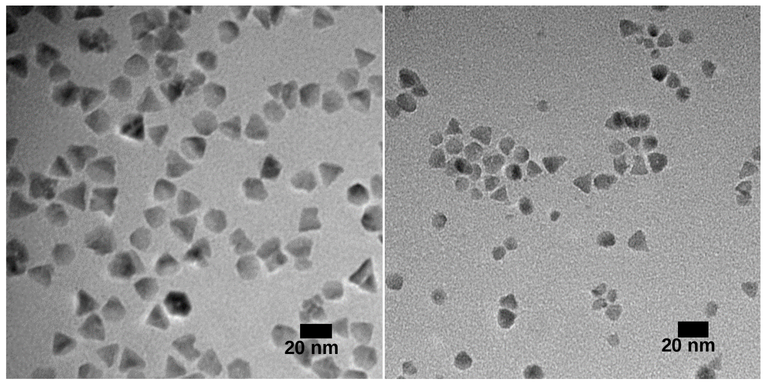

Figure 34. The TEM images of the Aluminum doped ZnO nanocrystals in this research. Scale bar 20nm.

here is whether there are surface charges in AZO nanocrystals or not, and how the surface charge and polarizability evolve from the undoped to the doped AZO. Through electrostatic force microscopy (EFM), we provided direct experimental evidence for the surface charges. Figure 35 shows the research theme of utilizing the EFM to detect surface charges in the AZO nanocrystals: the core-shell structure of AZO nanocrystal by etching-doping-regrowth, and the EFM probe and nanocrystal configuration.

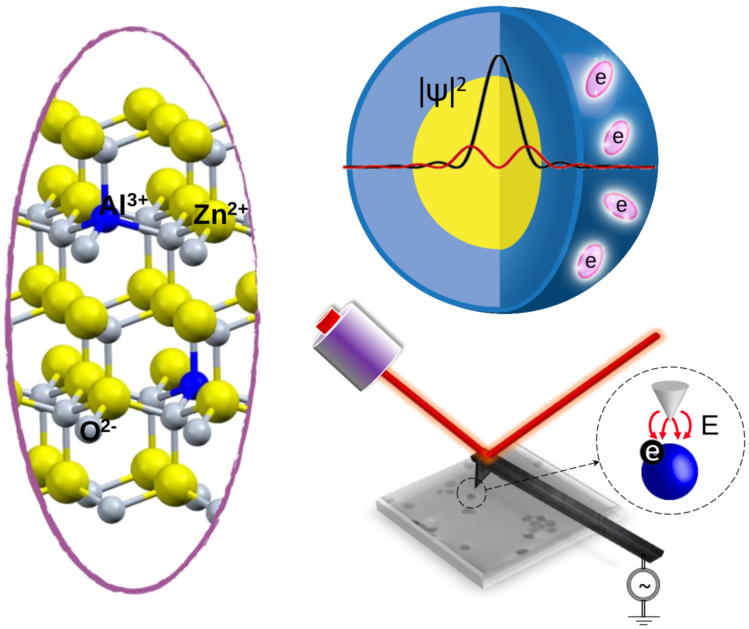

Figure 35. The research theme of utilizing the EFM to detect surface charges in AZO nanocrystals. Left portion shows the lattice structure of AZO. Upper-right shows the core-shell structure of AZO nanocrystal and the schematic wavefunction. Lower-right shows the EFM.

3.2 Experimental Approach

The aluminum doped ZnO (AZO) nanocrystals (NC), used as the material platform for this study, were synthesized by Dongming Zhou in the Kittilstved group, using a newly developed etching-regrowth-doping approach. The synthesis is summarized in Figure 36.

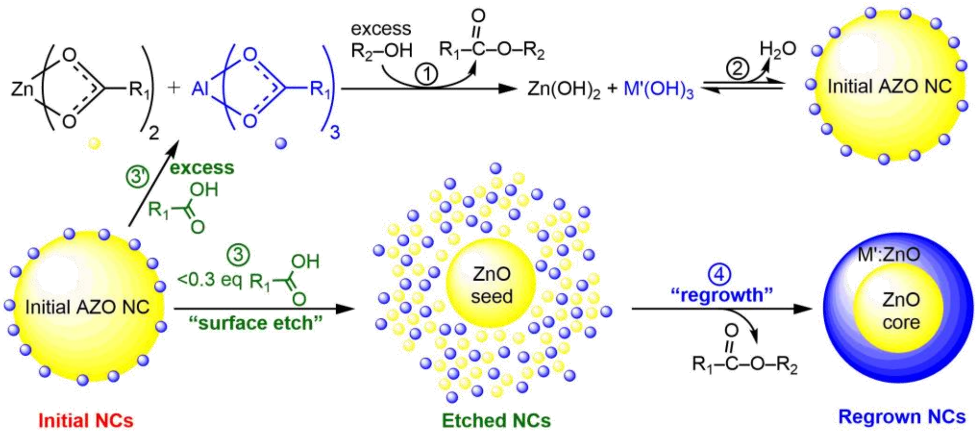

Figure 36. The synthesis steps of AZO nanocrystals, including mainly three steps: growing initial nanocrystals, etching, and regrowing. The yellow sphere stands for the ZnO seed, the blue shell stands for the doped part.

Briefly, using ZnO nanocrystals as a starting point, the NC surface was etched with the oleic acid. Nanocrystals were then activated and regrown with aluminum salts. This approach has achieved the highest percentages of active Al^{3+} dopants in AZO nanocrystals reported to date: ~10^2 conduction band electrons per NC. The high number of active dopants also ensured enough surface charges for this study.

I employed Electrostatic Force Microscopy (EFM) in an attempt to quantify the number of the surface charges and the nanocrystal polarizability after Al-doping. There have been multiple publications featuring the utilization of the EFM to explore charge transfer phenomena in organic photovoltaic systems.[51-53] Previous work in our laboratory using the EFM and the fluorescence imaging to quantify the surface charges in semiconductor quantum dots charged by electrospray..[54-55] The EFM is a variant of charge-force imaging, sensitive to both capacitive interactions and surface charge-electric field interactions between the metal-coated probe and surface species. The EFM is a multi-pass technique in which the sample is repeatedly scanned with varying tip bias (at fixed lift height), where the charge and the polarizability information is encoded in the relative shift of the resonance frequency or the phase of the cantilever with respect to the tip bias. Because the interactions act as an effective spring constant in equivalence, altering the oscillation of the cantilever. The change in resonance frequency can be thought of as a variation of the equivalent spring constant change due to the force field , which is given by

$$|\Delta\nu| = |\nu - \upsilon'| \approx \frac{\nu}{2k}\frac{\partial F}{\partial z}, \qquad (3.1),$$ [56]

where ν is the unaffected resonance frequency, $\upsilon'$is the influenced resonance frequency, z is the tip-substrate distance, k is the cantilever force constant, $\frac{\partial F}{\partial z}$is the z-force gradient.

The phase shift formula of the resonant peak versus the tip bias is

$$\Delta\Phi = A \cdot V_{EFM} + B \cdot V_{EFM}^2, \qquad (3.2),$$

where $\Delta\Phi$ is the phase shift of the resonant peak, V_{EFM} is the tip bias, and the coefficients A and B are given by, $A = \left[\frac{\Omega}{kz^2}\right]$q, $B = -\frac{\Omega}{k}\left[\frac{3\alpha}{z^4}\right]$, here Ω is the quality factor, the spring constant k=50N/m for AppNano probes used in this research , q is the surface charge, z=40nm is the lift height, and α is the polarizability, (the signs of phaseshift, A and B coefficients are flipped to make the parabolas opening upwards when plotting).[54] The first term is due to the force arising from the charge-electric field interaction and thus proportional to the tip bias V. The capacitive force is the derivative of the capacitive energy and thus the second term is proportional to V^2. The z dependence of coefficient B is determined by the geometry of the tip-object configuration. By fitting of the phase shift with respect to the tip bias to a parabolic function, and parsing the linear and quadratic components, the surface charge can be acquired by the linear component and the polarizability can be obtained by the quadratic component. The resolution of EFM falls around the size of nanocrystals; and possesses the high precision required to resolve down to 2~3 charges, making it a powerful tool for this study to provide direct experimental evidence for the surface charges in this nanocrystal system.

3.3 Results and discussions

The Aluminum-doped or undoped ZnO nanocrystals were deposited on the glass or the highly oriented pyrolytic graphite (HOPG). Figure 37 shows the phase-shift versus tip bias for the different scenarios, with the insets depicting the corresponding surface morphologies of NCs and height line-sections. In Figure 37a, the undoped NC on the glass has a linear component with a nearly zero slope (zero charge), while the Figure 37b highly activated doped NC (the regrowth is complete) on glass holds 91 surface

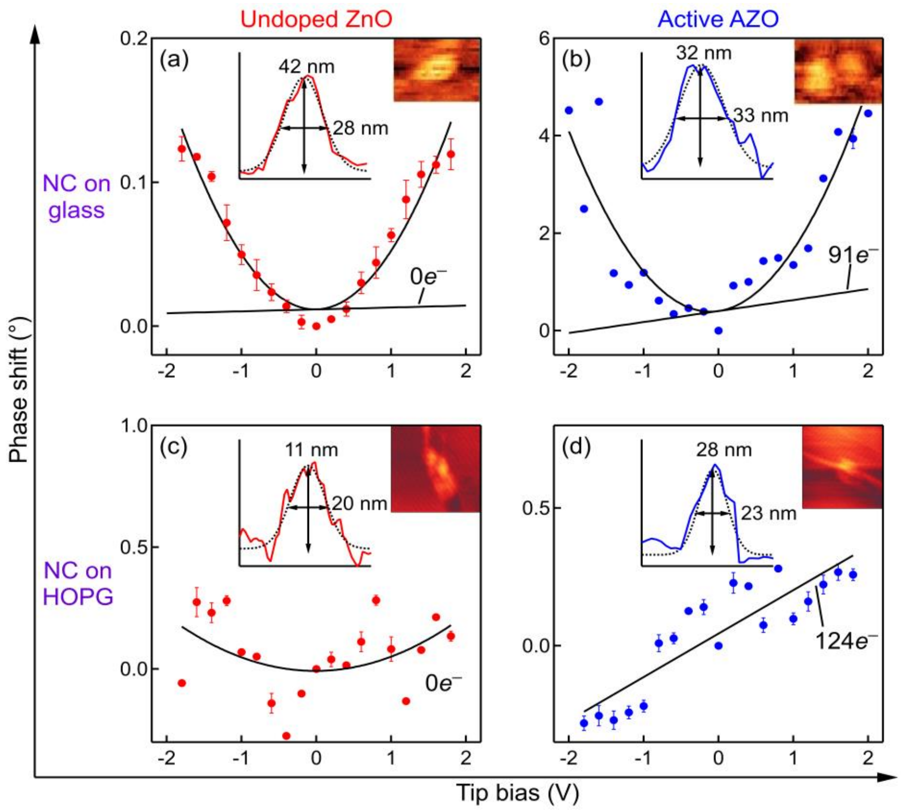

Figure 37. The phase shift with respect to the tip bias of nanocrystals in different scenarios: the undoped NC, the highly-activated doped NC on the glass or the highly-oriented-pyrolytic-graphite (HOPG). The insets show the AFM morphologies of nanocrystals and extracted height line profiles. The undoped ZnO NC on the glass, from the linear part, exhibit a surface charge of 0e-. The highly Activated doped ZnO NC on the glass reveals a 91e- surface charge. The surface charge of the NC on the HOPG is 0e-. The surface charge of the highly activated NC on the HOPG is 124e-.

charges. However, for the NC on the HOPG substrate, in contrast to the glass substrate case in which the quadratic term dominates, the linear term in the phase-shift becomes dominant. In Figure 37c, the phase-shift is very small for the undoped NC on the HOPG, presenting a very shallow parabola, which oscillates around 0. In Figure 37d, the phase-shift of the highly activated doped NC on the HOPG displays an almost dominant linear behavior. The calculated charge 124e- is in the same order of magnitude of that on the glass. The much smaller second order term implies that the second z-derivative of the tip-HOPG-NC capacitance, which the phaseshift is proportional to, is very small.[57]

According to T. Melin. et al, the tip-substrate interaction makes the

$\frac{d^2 C_{tip-substrate}}{dz^2}$ term scale as $z^{-\alpha}$, endowing the liftheight dependence of the phaseshift of the tip-substrate interaction, which is proportional to the third-order z derivative of $C_{tip\text{-}substrate}$, an

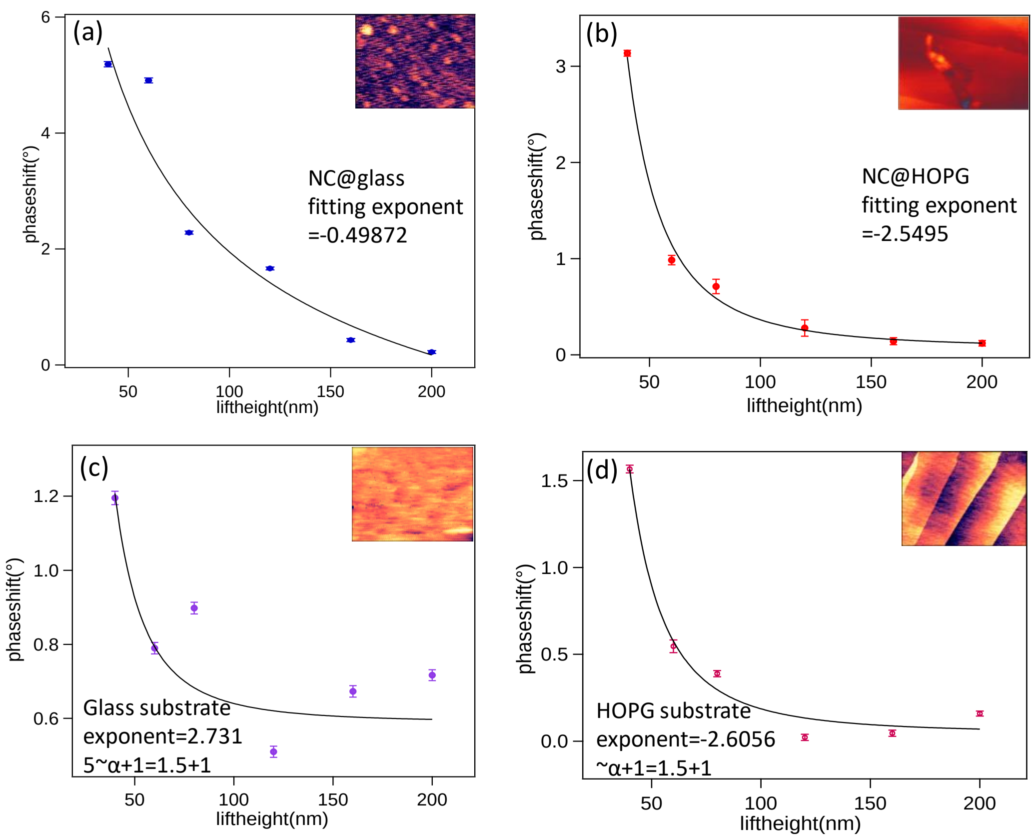

Figure 38. Lift-height dependence of the phaseshift of (a) the nanocrystal on glass, (b) the nanocrystal on HOPG, (c) the glass substrate, (d) the HOPG substrate. The inset images are the corresponding AFM images of NCs and substrates. The power number is the fitting power of phaseshift versus lift-height is close to –(β+1)

exponent of $-(\beta+1)$.[58] Typical value of β for substrates is 1.5.[58] In Figure 38c, d, the lift-height dependence of the phaseshift of tip-substrate has an exponent of around –(1.5+1), in good agreement with the literature report.

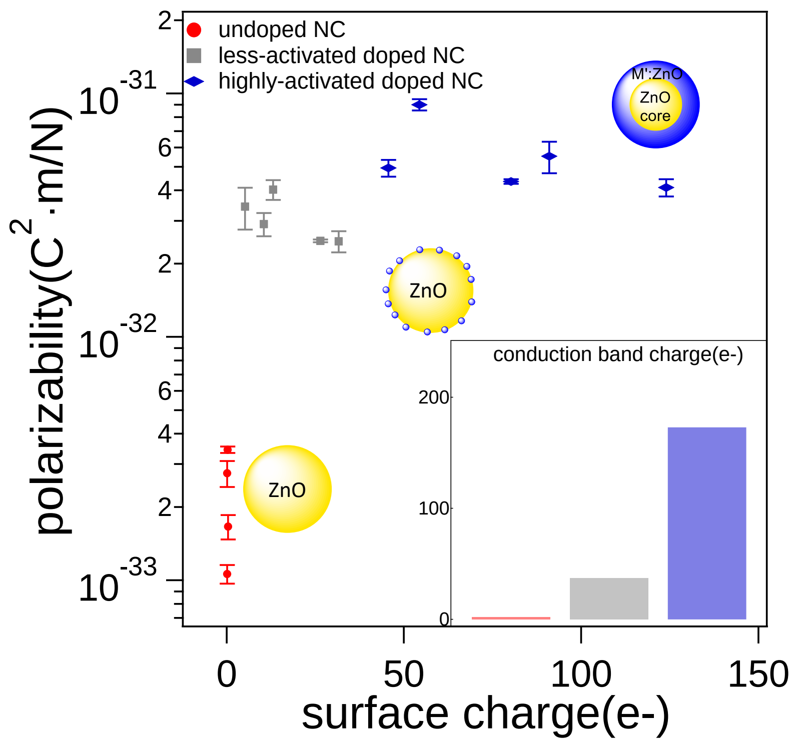

Figure 39. The polarizability-surface charge scatter plot comparing the undoped/highly-activated-doped/less-activated doped ZnO NCs deposited on the glass. The cartoons depict the respective nanocrystals. The active doped NC shows 50-150 surface charges. The less-activated doped NC shows below 50 surface charges. The undoped NC shows around 0 surface charges. The highly-activated doped NC has a polarizability slightly higher than that of less-activated doped NC, but order of magnitude higher than that of undoped NC. The inset is the bar chart for the numbers of the conduction band charge of NCs determined by plasmonic resonance.

In Figure 38a, b, the fitting exponent associated with the phase-shift versus the lift-height for the NCs on the glass and the HOPG also showed an interesting difference in the fitting exponent of the z dependence of the phaseshift, perhaps due to different tip-substrate-NC capacitive behavior on the two substrates, consistent with the different phaseshift pattern when changing tip bias. Figure 39 also shows the NC polarizability, extracted from the B coefficient, versus the surface charge for the groups of the undoped NC, the less-activated doped NC (the regrowth is initially started) and the highly-activated doped NC (the regrowth is complete). The inset shows a bar chart representing the number of conduction band charges estimated from the plasmon absorption by Zhou, aiming at giving a general impression about the comparison of magnitude and how the electrons are distributed among the surface and

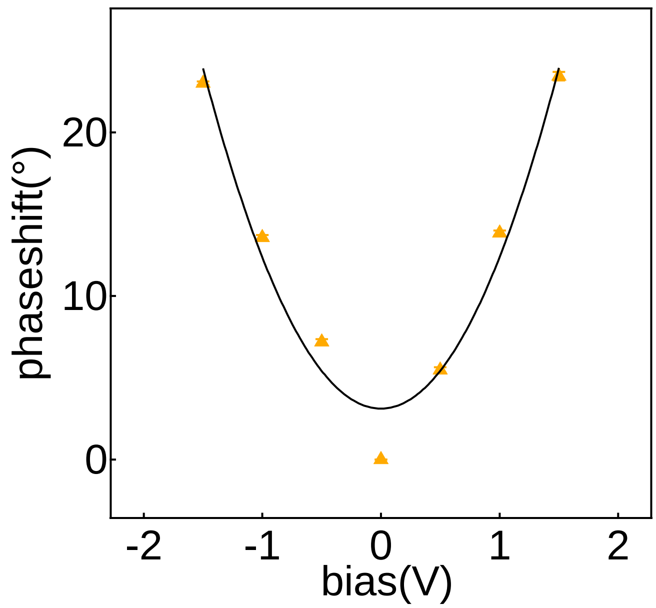

Figure 40. The phaseshift versus the tip bias for the gold nanoparticle. By fitting to parabolic function, the surface charge is 1e, the polarizability is α=7.33× 10^{-31}(C^2m/N).

conduction band. The highly-activated doped NC has a polarizability appreciably higher (1-2 order of magnitude) than that of the undoped NC and seems to present an upper limit in the sublinear trend. This upper-limit is reasonable because the doping will approach saturation, and according to the Clausius-Mossotti relation:

$$\frac{N\alpha}{3\varepsilon_0} = \frac{\varepsilon_r - 1}{\varepsilon_r + 2} = 1 - \frac{3}{\varepsilon_r + 2}, \qquad (3.3).$$

Here, N is the number density of the molecules, α is the molecular polarizability, ε_0 is the vacuum permittivity, ε_r is the dielectric constant of the material. There is an upper-limit for the right-hand-side of equation 3.3 and thus an upper-limit for polarizability is sensible. On the other hand, the less-activated doped NC has a slightly smaller polarizability than the highly-activated doped NC. The reason behind it might be: the polarizability has a direct link to dielectric constant (equation 3.3), rather than the conduction band electrons. After doping aluminum, the values of the nanocrystals' dielectric constants are closer, whether highly-activated or not, than the undoped ZnO ones. I also measured gold nanoparticles as a reference. By fitting in Figure 40, the gold nanoparticle possesses surface charge close to zero, confirming that we are measuring the surface charge, and a polarizability 1-2 order of magnitude higher than that of the highly-activated doped ZnO nanocrystals.

In support of this experimental work, Zhou obtained the band profile and the electron density profile (Figure 41) from solving the Poisson equation by substituting the electron density and taking into account of the Fermi-Dirac distribution, degeneracy.[59] The electron density profile shows an increase around the boundary. Though not direct detection of the surface charge, some other researchers utilized the time-resolved PL and the transient absorption on the CdSe quantum dots system and provided indirect experimental results about surface charges, supporting our results to some extent.[48, 50] They pointed out one possible source of the surface charge: electrons fill into the surface states. [48, 50]

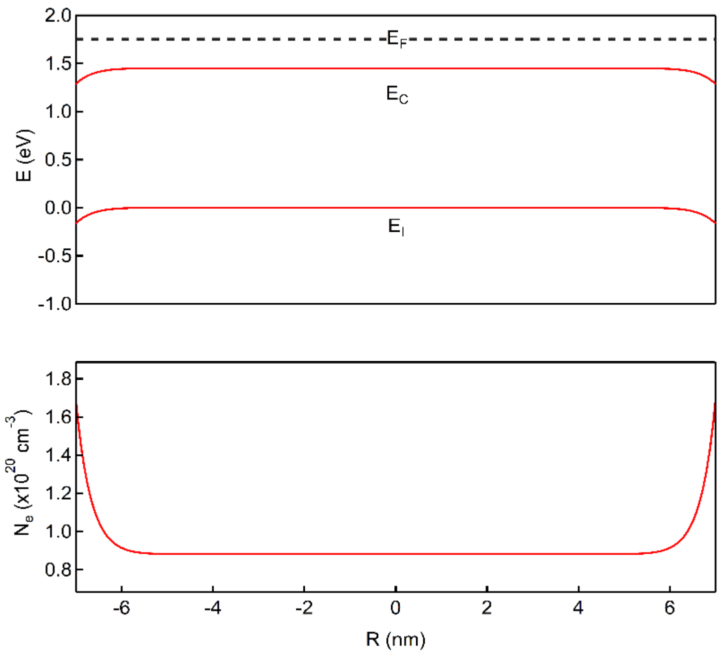

Figure 41. (Top) The calculated radial band profile by solving Poisson equation. (Bottom) The calculated Radial electron density profile. The tails see an increase in the density of electrons.

3.4 Conclusion

In summary, the investigation of the surface charges on the AZO NCs by the EFM revealed large numbers of negative charge carriers (100~200) on the NC surface, which is striking. For the NCs on the HOPG, the first order term in phase-shift versus bias dominates and is qualitatively different from the behavior of the same NCs on glass where the second order term in the phase-shift versus the tip-bias dominates. The highly activated doped NCs exhibit a polarizability 1-2 order of magnitude higher than that of the undoped NCs, and the less-activated doped NC has a polarizability slightly smaller than that of the highly activated doped NC. Because the charges are connected closely with the light emission dynamics,[48] the local surface plasmon resonances,[60] and the catalysis,[45] this study benefits the expansion of the utility of the AZO nanocrystals in these areas of NC-based optoelectronics.

CHAPTER 4

KPFM INVESTIGATION ON ORGANIC THERMOELECTRIC MATERIALS AND NANOIMPRINTED PROTEIN FILM

In this section, I will cover some sideline work about the organic thermoelectric materials and the nanoimprinted protein films.

4.1 Introduction and overview about the organic thermoelectric materials

Thermoelectric materials transform a heat flow into electricity, so called Seebeck effect. The thermoelectric energy conversion efficiency is measured as a figure-of-merit:

$$ZT = \frac{S^2\sigma T}{\kappa}, \qquad (4.1),$$

where S is the Seebeck coefficient, σ is the electrical conductivity, T is the absolute temperature, and κ is the thermal conductivity.[61] Since the Seebeck effect is discovered, this area remains lukewarm for nearly seventy years until the material bismuth telluride based alloys are discovered.[62] But the bismuth telluride is extremely expensive, rare and hard to obtain. Currently, science communities are exploring using organic materials such as the P3HT to be thermoelectric materials, due to numerous advantages like low cost, large-area deposition, high elasticity, material abundance and low weight.[61] In thermoelectric materials, an important parameter is so called charge-transport parameter s, which is the fitting power for conductivity versus the energy difference from transport edge.[63] Doping is key to maximize the thermoelectric performance, because it influences conductivity hence power factor $S^2\sigma$ in the numerator of the figure-of-merit, and affects carrier mobility. Previously, people thought the doping is a homogeneous process inside the material. We wanted to address the question that how does the density of states (DOS) change in material upon doping with respect to the charge transport parameter s, and investigated on the organic materials P3HT and PDDP4T, provided by the collaborator Connor Boyle in DV lab. The experimental setup is the combination of the KPFM and the PL: The KPFM is able to detect the electronic states in the film, manifested as the SPC; the PL provides a complementary method to verify the inhomogeneity as the highly-doped and the less-doped area show distinction in photoluminescence. After the experiments, striking inhomogeneity of DOS is discovered, contradictory to what people thought before. This study contributes to more thorough understanding of the charge transport process in organic thermoelectrics and is beneficial to efficiency enhancement.

4.2 Results and discussions about the KPFM study about the organic thermoelectric materials

We studied two kinds of thermoelectric organic materials: the P3HT and the PDPP4T when doped with the iodine at both the high temperature and the low temperature. As the parameter s

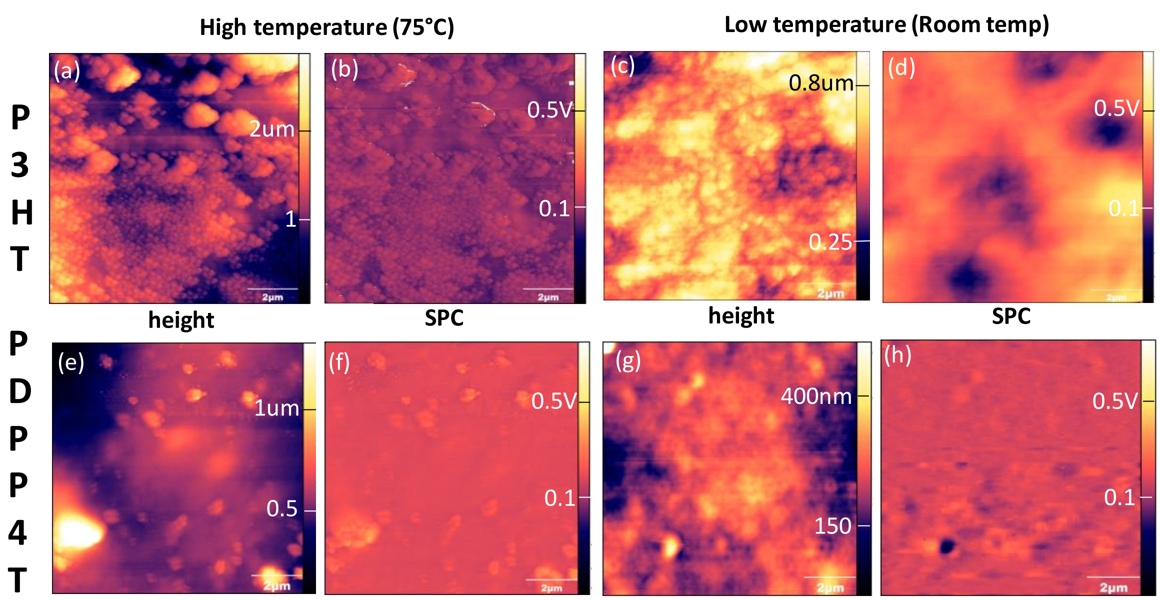

Figure 42. The surface height and the surface potential contrast images of the four scenarios: respectively the P3HT at the high temperature (75℃) (a)(b); the P3HT at the low temperature (room temperature) (c)(d); the PDPP4T at the high temperature (e)(f) and the PDPP4T at the low temperature (g)(h). The scales for SPC are all the same. The scale bars: 2um.

is defined before, the collaborator Connor Boyle found that at the low temperature (room temperature), the P3HT has an s=8.5; and at the high temperature (75℃), the P3HT has an s=6.5. Moreover, at the low temperature, the PDPP4T has an s=2; and at the high temperature, the PDPP4T has an s=0.5. We wanted to investigate the surface Density of States (DOS) on scenarios of different s and temperature through the KPFM because the surface potential results from electronic states. Figure 42 shows the KPFM scans of the P3HT and the PDPP4T at both the high temperature and the low temperature. The SPC image of the P3HT that has a high s=8.5 (Figure 42d) at the low temperature displays more inhomogeneity than the one has a lower s=6.5 at the high temperature (Figure 42b), the iodized/oxidized regions possess an SPC obviously lower than the other parts. Moreover, the PDPP4T at the low temperature reveals more inhomogeneity than that at the high temperature (Figure 42f, h), but still less inhomogeneous than that of the P3HT. At the high temperature, the SPC image is quite homogeneous (s=0.5) (Figure 42f).

Figure 43 shows the color-scaled images of the SPC channels from Figure 43, we can clearly

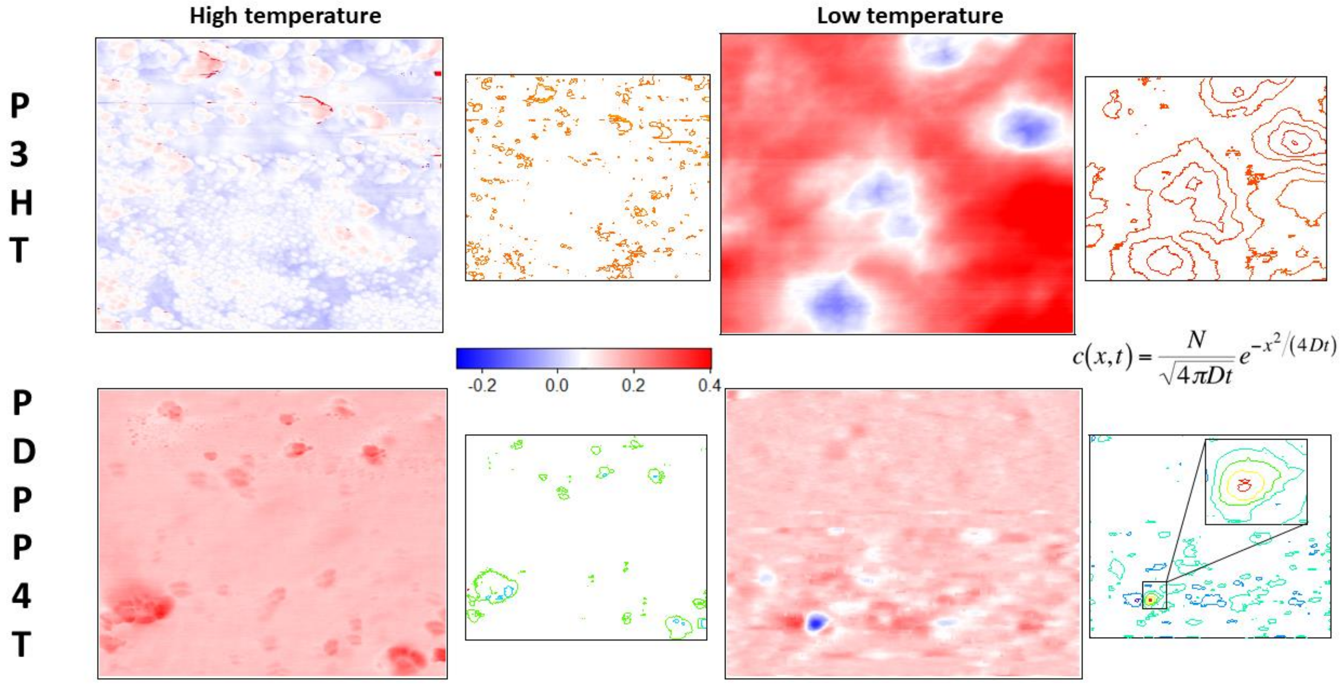

Figure 43. The color-scaled images of the SPC channels in Figure 43, associated with the contour plots. The color bar in the middle shows the color-code. The contour plots in the upper-right and the lower-right show the diffusion of the doping.

see the inhomogeneity in the P3HT is higher than that of the PDPP4T, and the low temperature shows a higher inhomogeneity than that of high temperature. Associated with the color-scaled images are the contour plots. If the diffusion and oxidation of the iodine obeys the diffusion equation

$$c(x,t) = \frac{N}{\sqrt{4\pi Dt}} \cdot \exp(-\frac{x^2}{4Dt}), \qquad (4.2).$$

Here N is the initial doping quantity, D is the diffusion coefficient, t is the time. The contour should show a two-dimensional Gaussian function. However, the contours in the upper-right and lower-right both show apparent distortion from a 2D Gaussian function. This further indicates the

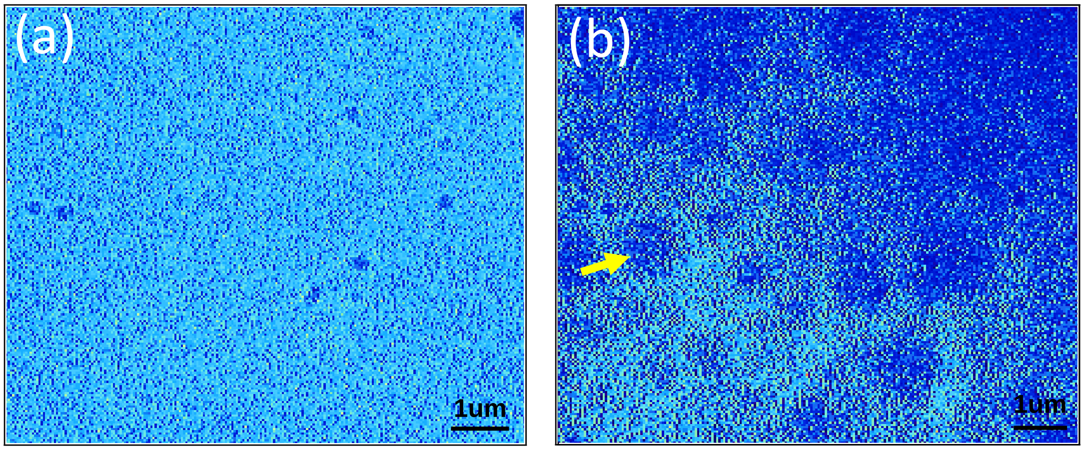

Figure 44. The PL images of (a) the pristine P3HT film, (b) the iodine doped P3HT film, the yellow arrow points to the clusters. Scale bar: 2um. The iodine doped P3HT film shows clear heterogeneity than the pristine P3HT film. Exposure time: 0.2s.

inhomogeneity in the process of doping. Furthermore, Figure 44 shows the PL images taken by camera on top for the pristine P3HT and the iodine-doped P3HT respectively, because the doped and the undoped P3HT have different PL intensities.[64] Figure 44b exhibits inhomogeneity after doping and some island-like features in the doping of the film, further confirming the inhomogeneity of DOS.

4.3 Conclusion about KPFM study about the organic thermoelectric materials

It reveals that contradictory to what people thought, the doping is an inhomogeneous process and different transport parameters show different degree of inhomogeneity. This work found what people did not thought of the DOS in thermoelectric organic material doping before, gained a more thorough understanding of the charge transport in organic thermoelectrics, and is impactful for improving the performance and the energy conversion efficiency of thermoelectric materials.

4.4 Results about the KPFM on biological system: the nanoimprinted protein film

The intrinsic structural and functional diversity inherent to proteins endow them highly versatile building blocks to nanobiology system. Protein films possess innate biocompatibility and processability to be applied to bioelectronics, tissue engineering and drug delivery.[65] Collaborators in Vincent Rotello group developed a nanoimprint lithography approach to fabricate robust protein film on gold substrates However, the answer to the question that whether the property of charge is kept in the process of

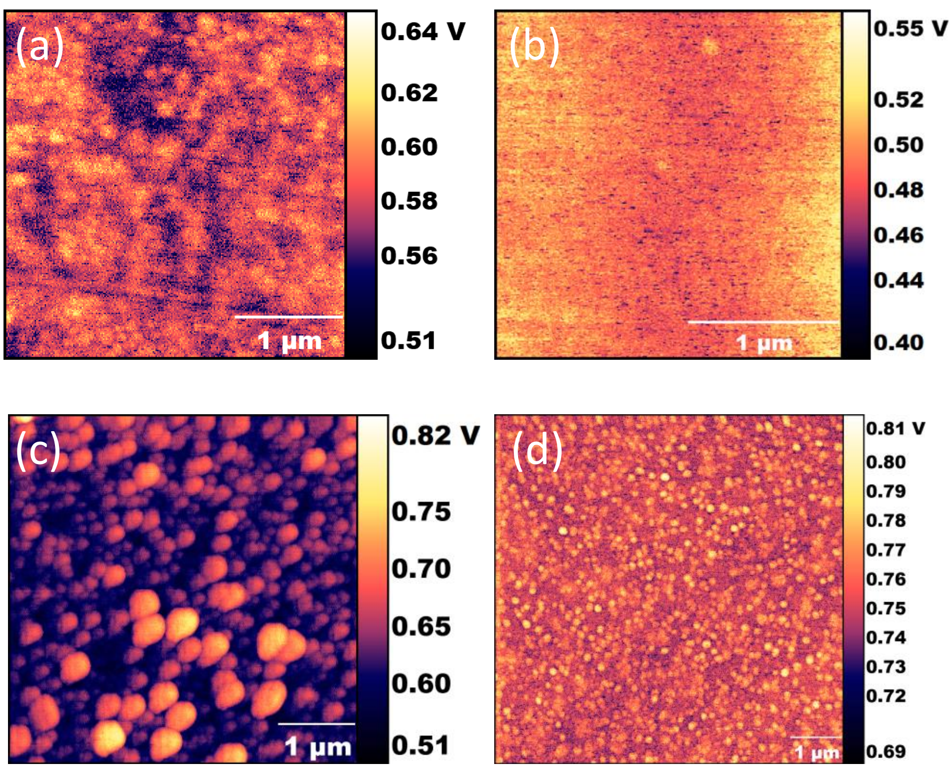

Figure 45. The SPC images of (a) the neutral gold substrate, (b) the bovine serum albumin, (c) the hemoglobin, (d) the lysozyme. The scale bars: 1um.

nanoimprinting is unknown. Using the Kelvin Probe Force Microscopy (KPFM), it is possible to give an answer about the type of charges in the film. The KPFM was conducted on a Digital Instrument atomic force microscope under probes with platinum coating (ANSCM-PA) purchased from AppNano. Figure 45 displays the SPC images of bare gold substrates and various protein films including the bovine serum albumin (BSA), the hemoglobin (Hb), and the lysozyme (lyso). Figure 46 extracts the SPC information in Figure 45 and made into histograms, displaying that the lyso has a higher SPC than the gold, the BSA has a lower SPC than the gold, and the Hb has an SPC more or less close to the gold, consistent with the positive charge in the lyso, negative charge in the BSA and neutral charge in the Hb, confirming the property of

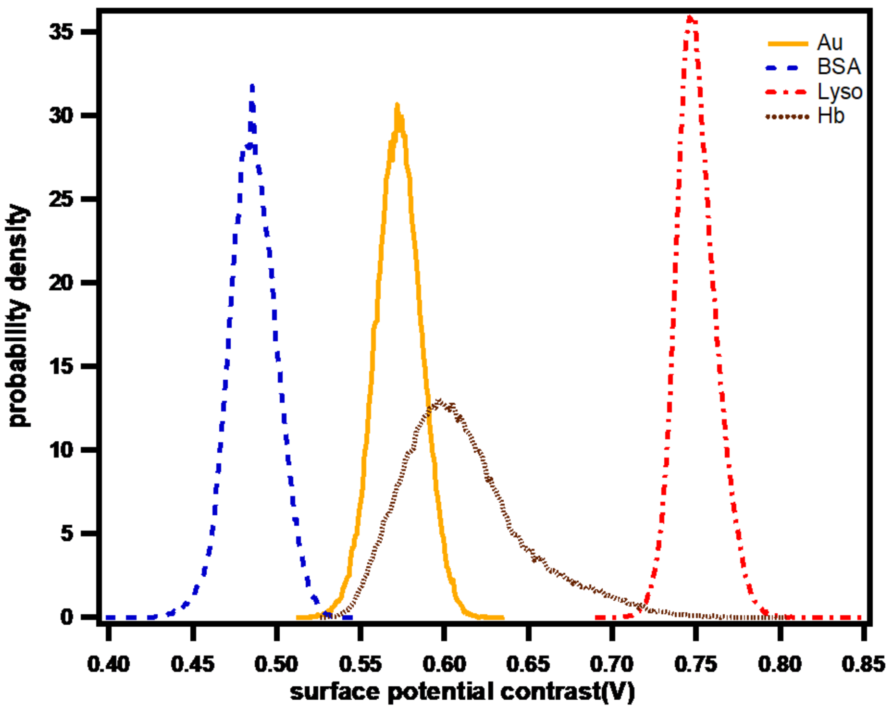

Figure 46. The histograms of the SPC extracted from the protein films in the Figure 45. The Au shows an SPC greater than the BSA, but smaller than the Lyso. The Hemoglobin has an SPC more or less close to that of the Au.

charge is kept in the nanoimprint. This work of probing the charge in nanoimprint protein film expands the application of KPFM into nanoimprint protein film system and was published on *Advanced Materials*.[65]

CHAPTER 5

CONCLUSION

Combining the KPFM (or the EFM) and the PL techniques, associated with other technique like transmission electron microscope (TEM), we investigated a variety of materials, including 1D TAT organic semiconductor nanowires, 2D transition metal dichalcogenides MoS_2, aluminum doped ZnO nanocrystals (AZO) and organic thermoelectric materials (P3HT, PDPP4T). We discovered way to disentangle the “bright” couplings and the “dark” couplings in organic semiconductor and tested the coupling theory. The good agreement between the experimental value and the theoretical simulated value shows how well the theoretical investigation can guide the experimental exploration. By the insights we gained, it is possible to modulate the packing motifs to tailor the electronic properties of the organic semiconductor. Moreover, we doped MoS_2 and found the bidirectional work function tuning with great tunability by non-covalent chemical doping, noting that organic p-doping is typically difficult to achieve, and based on the substrate dependence of SPC change, we proposed a physical picture of co-effect of the charge transfer dipoles and the interfacial dipoles for an explanation and we know other than the dopants, the substrate also deserve a consideration in the MoS_2 work function engineering. This study also showed how high-level computational calculation can benefit the rational design of the electronic properties of TMDCs. We also employed the EFM to study the surface charge which is not known before in the AZO nanocrystals and found high number of doped charges, remarking the small size (~20nm). Besides, employing KPFM to study the density of states in the thermoelectric materials, during doping the iodine and oxidation, the inhomogeneity in the density of states was revealed, which is contradictory to what peoples thought previously. This help people to gain more thorough insights into the charge transport in organic thermoelectrics. Last but not least, we also studied biological system such as the protein film and verify the properties of charge in the proteins. Through these varieties of works, the power of the combination of KPFM and PL techniques was demonstrated, and we gained insights for optimizing and functionalization of organic semiconductor devices, greater tunability of TMDCs for the scalable integration into electronics, the potential utilities of nanocrystals, and the energy conversion efficiency enhancement of the organic thermoelectric materials.

CHAPTER 6

FUTURE DIRECTIONS

First, we have studied the effect of ground state CT interaction on the work function of TAT seminally. A generalization and expansion are awaiting exploration. The room temperature charge mobility of the most conductive organic semiconductors such as the rubrene or the pentacene reaches a few tens of $cm^2 \cdot V^{-1} \cdot s^{-1}$, and some even reports the single crystal bulk mobility can achieve $100cm^2 \cdot V^{-1} \cdot s^{-1}$,[66] making them promising systems for the directional energy and charge transport.[67] How does the ground state interactions influence the rubrene or pentacene's electronic and optoelectronic properties remain an interesting and meaningful question, and is helpful to improve directional energy and charge transport through modulating the coupling energy through packing motifs. The similar investigation can be expanded into the rubrene or pentacene.

Second, perovskite solar cells have recently reached certified power conversion efficiencies of 20.1% due to their superior charge carrier mobilities and the low densities of deep trap states.[68] Within a short period of time (six years),[69] it achieved an efficiency boost and now it became the hottest area of the photovoltaic application. After coating with the electron or hole transport layer, how does the hydrophobicity change on the materials is an interesting research question, because the moist have a great impact on the devices in a real environment. After self-assembling a layer of Trichloro(hexyl)silane on silicon probe readily, the probe becomes hydrophobic and by scanning through the layer, the phase image can tell the hydrophobicity of the layer due to the attractive or repulsive force because of hydrophobicity. Hence, we can map hydrophobicity of the charge transport layer and see how it changes in the humidity and impact the material performance.

Third, zwitterions, are molecules with two or more functional groups, of which at least one has a positive and one has a negative electrical charge and the net charge of the entire molecule is zero. We have gained some knowledge about the doping effect of the molecules have just electron donating or accepting group. How doping the MoS_2 with the zwitterions with both positive and negative charges influence the work function of TMDCs, is worth exploring.

Collaborators in Emrick group can prepare zwitterion and they already did some research on the effect of zwitterion on graphene FET devices. The doping procedures should be close to the experiments described in this research, while the outcome is intriguing and worth investigating.

REFERENCES

1. Fan, J.; Zhang, L.; Alejandro, B.; Fred, W., Synthesis and Characterization of 7,8,15,16-Tetraazaterrylene. *Organic Letters* 2012, **14** (4), 1024-1026.

2. Spano, F. C.; Silva, C., H- and J-aggregate behavior in polymeric semiconductors. *Annu Rev Phys Chem* 2014, **65**, 477-500.

3. Zhang, J.; Xu, W.; Sheng, P.; Zhao, G.; Zhu, D., Organic Donor-Acceptor Complexes as Novel Organic Semiconductors. *Acc Chem Res* 2017, **50** (7), 1654-1662.

4. Nielsen, C. B.; Holliday, S.; Chen, H. Y.; Cryer, S. J.; McCulloch, I., Non-fullerene electron acceptors for use in organic solar cells. *Acc Chem Res* 2015, **48** (11), 2803-12.

5. Heremans, P.; David, C.; Barry, R., Strategies for Increasing the Efficiency of Heterojunction Organic Solar Cells: Material Selection and Device Architecture. *Accounts of Chemical Research* 2009, **42**, 1740-1747.

6. Simon, G.; Rao, A.; Kumar, A.; Smith, S.; Chin, A.; Clark, J.; van der Poll, T.; Bazan, G.; Friend, R., Ultrafast Long-Range Charge Separation in Organic Semiconductor Photovoltaic Diodes. *Science* 2014, **343**, 512-516.

7. Forrest, S., The path to ubiquitous and low-cost organic electronic appliances on plastic. *Nature* 2004, **428**, 911-918.

8. Uoyama, H.; Goushi, K.; Shizu, K.; Nomura, H.; Adachi, C., Highly efficient organic light-emitting diodes from delayed fluorescence. *Nature* 2012, **492** (7428), 234-8.

9. Hestand, N. J.; Spano, F. C., Molecular Aggregate Photophysics beyond the Kasha Model: Novel Design Principles for Organic Materials. *Acc Chem Res* 2017, **50** (2), 341-350.

10. Yamagata, H.; Pochas, C. M.; Spano, F. C., Designing J- and H-aggregates through wave function overlap engineering: applications to poly(3-hexylthiophene). *J Phys Chem B* 2012, **116** (49), 14494-503.

11. Yamagata, H.; Maxwell, D. S.; Fan, J.; Kittilstved, K. R.; Briseno, A. L.; Barnes, M. D.; Spano, F. C., HJ-Aggregate Behavior of Crystalline 7,8,15,16-Tetraazaterrylene: Introducing a New Design Paradigm for Organic Materials. *The Journal of Physical Chemistry C* 2014, **118** (49), 28842-28854.

12. Yan, W.; Li, Y.; Ye, S.; Li, Y.; Rao, H.; Liu, Z.; Wang, S.; Bian, Z.; Huang, C., Increasing open circuit voltage by adjusting work function of hole-transporting materials in perovskite solar cells. *Nano Research* 2016, **9** (6), 1600-1608.

13. Hestand, N.; Spano, F. C., Interference between Coulombic and CT-mediated couplings in molecular aggregates: H- to J-aggregate transformation in perylene-based pi stacks. *Journal of Chemical Physics* 2015, **143**, 244707, 1-16.

14. Baghgar, M.; Barnes, M. D., Work Function Modification in P3HT H/J Aggregate Nanostructures Revealed by Kelvin Probe Force Microscopy and Photoluminescence Imaging. *ACS nano* 2015, **9**, 7105-7112.

15. Palermo, V.; Palma, M.; Samorì, P., Electronic Characterization of Organic Thin Films by Kelvin Probe Force Microscopy. *Advanced Materials* 2006, **18** (2), 145-164.

16. Melitz, W.; Shen, J.; Kummel, A. C.; Lee, S., Kelvin probe force microscopy and its application. *Surface Science Reports* 2011, **66** (1), 1-27.

17. Wise, A. J.; Zhang, Y.; Fan, J.; Wudl, F.; Briseno, A. L.; Barnes, M. D., Spectroscopy of discrete vertically oriented single-crystals of n-type tetraazaterrylene: understanding the role of defects in molecular semiconductor photovoltaics. *Phys Chem Chem Phys* 2014, **16** (30), 15825-30.

18. Yi, H. T.; Gartstein, Y. N.; Podzorov, V., Charge carrier coherence and Hall effect in organic semiconductors. *Sci Rep* 2016, **6**, 23650.

19. Kobayashi, S.; Nishikawa, T.; Takenobu, T.; Mori, S.; Shimoda, T.; Mitani, T.; Shimotani, H.; Yoshimoto, N.; Ogawa, S.; Iwasa, Y., Control of carrier density by self-assembled monolayers in organic field-effect transistors. *Nat Mater* 2004, **3** (5), 317-22.

20. Fan, J.; Li, T.; Djerdj, I., Two-Dimensional Atomic Crystals: Paving New Ways for Nanoelectronics. *Journal of Electronic Materials* 2015, **44** (11), 4080-4097.

21. Giannazzo, F.; Fisichella, G.; Greco, G.; Di Franco, S.; Deretzis, I.; La Magna, A.; Bongiorno, C.; Nicotra, G.; Spinella, C.; Scopelliti, M.; Pignataro, B.; Agnello, S.; Roccaforte, F., Ambipolar MoS2 Transistors by Nanoscale Tailoring of Schottky Barrier Using Oxygen Plasma Functionalization. *ACS Appl Mater Interfaces* 2017, **9** (27), 23164-23174.

22. Zhang, Z.-X.; Li, D., Novel p-n junctions based on ambipolar two-dimensional crystals. *Acta Physica Sinica* 2017, **66** (21), 217302, 1-13.

23. Radisavljevic, B.; Radenovic, A.; Brivio, J.; Giacometti, V.; Kis, A., Single-layer MoS2 transistors. *Nat Nanotechnol* 2011, **6** (3), 147-50.

24. Ryder, C. R.; Wood, J. D.; Wells, S. A.; Hersam, M. C., Chemically Tailoring Semiconducting Two-Dimensional Transition Metal Dichalcogenides and Black Phosphorus. *ACS Nano* 2016, **10** (4), 3900-17.

25. Mei, Y.; Fogel, D.; Chen, J.; Ward, J. W.; Payne, M. M.; Anthony, J. E.; Jurchescu, O. D., Interface engineering to enhance charge injection and transport in solution-deposited organic transistors. *Organic Electronics* 2017, **50**, 100-105.

26. Lanzillo, N. A.; Simbeck, A. J.; Nayak, S. K., Strain engineering the work function in monolayer metal dichalcogenides. *J Phys Condens Matter* 2015, **27** (17), 175501.

27. Li, F.; Qi, J.; Xu, M.; Xiao, J.; Xu, Y.; Zhang, X.; Liu, S.; Zhang, Y., Layer Dependence and Light Tuning Surface Potential of 2D MoS2 on Various Substrates. *Small* 2017, **13** (14).

28. Zhang, Q.; Chen, Y.; Zhang, C.; Pan, C. R.; Chou, M. Y.; Zeng, C.; Shih, C. K., Bandgap renormalization and work function tuning in MoSe2/hBN/Ru(0001) heterostructures. *Nat Commun* 2016, **7**, 13843.

29. Sim, D. M.; Kim, M.; Yim, S.; Choi, M.-J.; Choi, J.; Yoo, S.; Jung, Y. S., Controlled Doping of Vacancy-Containing Few-Layer MoS2 via Highly Stable Thiol-Based Molecular Chemisorption. *ACS Nano* 2015, **9** (12), 12115-12123.

30. Alon, H.; Stern, C.; Kirshner, M.; Sinai, O.; Wasserman, M.; Selhorst, R.; Gasper, R.; Ramasubramaniam, A.; Emrick, T.; Naveh, D., Lithographically Patterned Functional Polymer-Graphene Hybrids for Nanoscale Electronics. *ACS Nano* 2018, **12** (2), 1928-1933.

31. Liscio, A.; Bonini, M.; Treossi, E.; Orgiu, E.; Kastler, M.; Dötz, F.; Palermo, V.; Samorì, P., Improving charge transport in poly(3-hexylthiophene) transistors via blending with an alkyl-substituted phenylene-thiophene-thiophene-phenylene molecule. *Journal of Polymer Science Part B: Polymer Physics* 2012, **50** (9), 642-649.

32. Liscio, A.; Palermo, V.; Fenwick, O.; Braun, S.; Mullen, K.; Fahlman, M.; Cacialli, F.; Samori, P., Local surface potential of pi-conjugated nanostructures by Kelvin probe force microscopy: effect of the sampling depth. *Small* 2011, **7** (5), 634-9.

33. Liscio, A.; Palermo, V.; Samori, P., Nanoscale Quantitative Measurement of the Potential of Charged Nanostructures by Electrostatic and Kelvin Probe Force Microscopy: Unraveling Electronic Processes in Complex Materials. *Accounts of Chemical Research* 2010, **43**, 541-550.

34. Wang, H.; Yu, L.; Lee, Y. H.; Shi, Y.; Hsu, A.; Chin, M. L.; Li, L. J.; Dubey, M.; Kong, J.; Palacios, T., Integrated circuits based on bilayer MoS(2) transistors. *Nano Lett* 2012, **12** (9), 4674-80.

35. Jariwala, D.; Sangwan, V.; Lauhon, L.; Marks, T. J.; Hersam, M. C., Emerging Device Applications for Semiconducting Two-Dimensional Transition Metal Dichalcogenides. *ACS Nano* 2014, **8**, 1102-1120.

36. Mouri, S.; Miyauchi, Y.; Matsuda, K., Tunable photoluminescence of monolayer MoS(2) via chemical doping. *Nano Lett* 2013, **13** (12), 5944-8.

37. Eda, G.; Yamaguchi, H.; Voiry, D.; Fujita, T.; Chen, M.; Chhowalla, M., Photoluminescence from chemically exfoliated MoS2. *Nano Lett* 2011, **11** (12), 5111-6.

38. Selhorst, R. C.; Puodziukynaite, E.; Dewey, J. A.; Wang, P.; Barnes, M. D.; Ramasubramaniam, A.; Emrick, T., Tetrathiafulvalene-containing polymers for simultaneous non-covalent modification and electronic modulation of MoS2 nanomaterials. Chemical *Science* 2016, **7** (7), 4698-4705.

39. Fang, H.; Tosun, M.; Seol, G.; Chang, T. C.; Takei, K.; Guo, J.; Javey, A., Degenerate n-doping of few-layer transition metal dichalcogenides by potassium. *Nano Lett* 2013, **13** (5), 1991-5.

40. Li, Y.; Qi, Z.; Liu, M.; Wang, Y.; Cheng, X.; Zhang, G.; Sheng, L., Photoluminescence of monolayer MoS2 on LaAlO3 and SrTiO3 substrates. *Nanoscale* 2014, **6** (24), 15248-54.

41. Jeong, K. S.; Deng, Z.; Keuleyan, S.; Liu, H.; Guyot-Sionnest, P., Air-Stable n-Doped Colloidal HgS Quantum Dots. *J Phys Chem Lett* 2014, **5** (7), 1139-43.

42. Krupka, J.; Derzakowski, K.; Tobar, M.; Hartnett, J.; Geyer, R. G., Complex permittivity of some ultralow loss dielectric crystals at cryogenic temperatures. *Measurement Science and Technology* 1999, **10** (5), 387-392.

43. Rong, L.-m.; Meng, Z.-j.; Xiao, C.; Zhou, L.; Du, L.-h.; Liu, K.; Du, J.-f., Impact of defects on local optical dielectric properties of Si/SiO2 interfaces by layered capacitor modeling. *Applied Physics A* 2016, **122** (4), 1-8.

44. Ko, D. K.; Urban, J. J.; Murray, C. B., Carrier distribution and dynamics of nanocrystal solids doped with artificial atoms. *Nano Lett* 2010, **10** (5), 1842-7.

45. Agrawal, A.; Cho, S. H.; Zandi, O.; Ghosh, S.; Johns, R. W.; Milliron, D. J., Localized Surface Plasmon Resonance in Semiconductor Nanocrystals. *Chem Rev* 2018, **118**, 3121-3207.

46. Casini, M., Active dynamic windows for buildings: A review. *Renewable Energy* 2018, **119**, 923-934.

47. Schimpf, A. M.; Knowles, K. E.; Carroll, G. M.; Gamelin, D. R., Electronic doping and redox-potential tuning in colloidal semiconductor nanocrystals. *Acc Chem Res* 2015, **48** (7), 1929-37.

48. Quinn, S. D.; Rafferty, A.; Dick, E.; Morten, M. J.; Kettles, F. J.; Knox, C.; Murrie, M.; Magennis, S. W., Surface Charge Control of Quantum Dot Blinking. *The Journal of Physical Chemistry C* 2016, **120** (34), 19487-19491.

49. Liu, H.; Brozek, C. K.; Sun, S.; Lingerfelt, D. B.; Gamelin, D. R.; Li, X., A Hybrid Quantum-Classical Model of Electrostatics in Multiply Charged Quantum Dots. *The Journal of Physical Chemistry C* 2017, **121** (46), 26086-26095.

50. Zeng, Y.; Kelley, D. F., Surface Charging in CdSe Quantum Dots: Infrared and Transient Absorption Spectroscopy. *The Journal of Physical Chemistry C* 2017, **121** (30), 16657-16664.

51. Coffey, D. C.; Ginger, D. S., Time-resolved electrostatic force microscopy of polymer solar cells. *Nat Mater* 2006, **5** (9), 735-40.

52. Cox, P. A.; Glaz, M. S.; Harrison, J. S.; Peurifoy, S. R.; Coffey, D. C.; Ginger, D. S., Imaging Charge Transfer State Excitations in Polymer/Fullerene Solar Cells with Time-Resolved Electrostatic Force Microscopy. *J Phys Chem Lett* 2015, **6** (15), 2852-8.

53. Giridharagopal, R.; Cox, P. A.; Ginger, D. S., Functional Scanning Probe Imaging of Nanostructured Solar Energy Materials. *Acc Chem Res* 2016, **49** (9), 1769-76.

54. Yalcin, S. E.; Labastide, J. A.; Sowle, D. L.; Barnes, M. D., Spectral properties of multiply charged semiconductor quantum dots. *Nano Lett* 2011, **11** (10), 4425-30.

55. Yalcin, S. E.; Yang, B.; Labastide, J. A.; Barnes, M. D., Electrostatic Force Microscopy and Spectral Studies of Electron Attachment to Single Quantum Dots on Indium Tin Oxide Substrates. *The Journal of Physical Chemistry C* 2012, **116** (29), 15847-15853.

56. Oksana, C.; Chen, L.; Weng, V.; Yuditsky, L.; Brus, L. E., Quantitative Noncontact Electrostatic Force Imaging of Nanocrystal Polarizability. *Journal of Physical Chemistry B* 2003, **107**, 1525-1531.

57. Lu, Y.; Munoz, M.; Steplecaru, C. S.; Hao, C.; Bai, M.; Garcia, N.; Schindler, K.; Esquinazi, P., Electrostatic force microscopy on oriented graphite surfaces: coexistence of insulating and conducting behaviors. *Phys Rev Lett* 2006, **97** (7), 076805.

58. Mélin, T.; Diesinger, H.; Deresmes, D.; Stiévenard, D., Electric force microscopy of individually charged nanoparticles on conductors: An analytical model for quantitative charge imaging. *Physical Review B* 2004, **69** (3), 035321.

59. Seiwatz, R.; Green, M., Space Charge Calculations for Semiconductors. *Journal of Applied Physics* 1958, **29** (7), 1034-1040.

60. Alina, S.; Niket, T.; Carolyn, G.; David, M.; Gamelin, D. R., Charge-Tunable QuantumPlasmons in Colloidal Semiconductor Nanocrystals. *ACS nano* 2014, **8**, 1065-1072.

61. Kim, G. H.; Shao, L.; Zhang, K.; Pipe, K. P., Engineered doping of organic semiconductors for enhanced thermoelectric efficiency. *Nat Mater* 2013, **12** (8), 719-23.

62. Bubnova, O.; Khan, Z. U.; Malti, A.; Braun, S.; Fahlman, M.; Berggren, M.; Crispin, X., Optimization of the thermoelectric figure of merit in the conducting polymer poly(3,4-ethylenedioxythiophene). *Nat Mater* 2011, **10** (6), 429-33.

63. Kang, D., Snyder, Jeffrey,, Charge-transport model for conducting polymers. *Nat Mater* 2017, **16** (2), 252-257.

64. Jenkins, J. L.; Lee, P. A.; Nebesny, K. W.; Ratcliff, E. L., Systematic electrochemical oxidative doping of P3HT to probe interfacial charge transfer across polymer–fullerene interfaces. *J. Mater. Chem. A* 2014, **2** (45), 19221-19231.

65. Jeoung, E.; Duncan, B.; Wang, L. S.; Saha, K.; Subramani, C.; Wang, P.; Yeh, Y. C.; Kushida, T.; Engel, Y.; Barnes, M. D.; Rotello, V. M., Fabrication of Robust Protein Films Using Nanoimprint Lithography. *Adv Mater* 2015, **27** (40), 6251-5.

66. Troisi, A., Charge transport in high mobility molecular semiconductors: classical models and new theories. *Chem Soc Rev* 2011, **40** (5), 2347-58.

67. Sakanoue, T.; Sirringhaus, H., Band-like temperature dependence of mobility in a solution-processed organic semiconductor. *Nat Mater* 2010, **9** (9), 736-40.

68. Yuan, M.; Quan, L. N.; Comin, R.; Walters, G.; Sabatini, R.; Voznyy, O.; Hoogland, S.; Zhao, Y.; Beauregard, E. M.; Kanjanaboos, P.; Lu, Z.; Kim, D. H.; Sargent, E. H., Perovskite energy funnels for efficient light-emitting diodes. *Nat Nanotechnol* 2016, **11** (10), 872-877.

69. Kutes, Y.; Zhou, Y.; Bosse, J. L.; Steffes, J.; Padture, N. P.; Huey, B. D., Mapping the Photoresponse of CH3NH3PbI3 Hybrid Perovskite Thin Films at the Nanoscale. *Nano Lett* 2016, **16** (6), 3434-41.